INORGANIC CHEMISTRY FRONTIERS

CCS 中国化学会 CHINESE CHEMICAL SOCIETY

ROYAL SOCIETY OF CHEMISTRY

Tuning Photoluminescence Properties of Au Clusters by Surface Modification and Doping: Lessons from Case Studies of Icosahedral Au_{13}

Journal:	*Inorganic Chemistry Frontiers*
Manuscript ID	QI-REV-07-2024-001773.R1
Article Type:	Review Article
Date Submitted by the Author:	05-Sep-2024
Complete List of Authors:	Buschmann, Dennis; The University of Tokyo, Department of Chemistry, Graduate School of Science Hirai, Haru; The University of Tokyo, Department of Chemistry, School of Science Tsukuda, Tatsuya; The University of Tokyo, Department of Chemistry, School of Science

SCHOLARONE™
Manuscripts

REVIEW

Tuning Photoluminescence Properties of Au Clusters by Surface Modification and Doping: Lessons from Case Studies of Icosahedral Au_{13}

Received 00th January 20xx,
Accepted 00th January 20xx

DOI: 10.1039/x0xx00000x

Dennis Alexander Buschmann,[ab] Haru Hirai,[a] and Tatsuya Tsukuda*[ab]

The photoluminescence (PL) properties of monolayer-protected gold nanoclusters (Au MPCs) have been extensively studied due to their wide range of potential applications, such as photocatalysis, photosensitization, bioimaging, and tumor therapy. The key factor that determines the PL properties of Au MPCs is the Au core size, but other parameters such as surface modifications and doping also significantly affect the PL properties. To understand and highlight the importance of these secondary parameters on the PL properties, this review article focuses on the ubiquitous icosahedral Au_{13} core as a benchmark and addresses the question of how the PL properties are affected by surface modification with X-type (thiolates, alkynyls) and L-type (phosphines, N-heterocyclic carbenes) ligands and doping with heterometals (Ru, Rh, Ir, Ni, Pd, Pt, Ag, Cd). The PL emission energy of Au_{13} MPC can be varied in the wide range of 1.1–2.1 eV and PL quantum yields up to 70% can be achieved by appropriate surface modification and doping. Based on the publications available until June 2024, the following empirical rules are derived to tune the PL emission energy and increase the PL quantum yield:

(1) The PL emission energy and PL quantum yield can be increased by using L-type ligands and/or doping with small group elements such as Ir, Pt, Ru, and Rh.

(2) The PL quantum yield can be enhanced by maximizing the interaction between the ligands through π···π or C-H···π interaction, chemical bonding, and steric packing.

The first rule follows the energy gap law and can be understood qualitatively by simple schemes based on the jellium model. The last rule is due to the suppression of non-radiative decay by the stiffening of the Au core. We hope that this review will help the audience to establish rational guidelines for designed PL properties.

1. Introduction

For decades, monolayer-protected gold clusters (Au MPCs) have attracted materials science researchers for two main reasons: (1) they exhibit new physicochemical properties not found in the corresponding bulk or nanoparticles (NPs); (2) their properties can be tuned over a wide range by changing the number of constituent atoms.[1-10] The origins for size-specific photophysical[11-22] and catalytic[23–29] properties are the unique atomic packing and quantized electronic structures of the Au cluster cores.

Photoluminescence (PL) is one of the size-specific properties of Au MPCs arising from direct consequences of quantized electronic structures.[30] The Au NPs and bulk Au do not exhibit intense PL because non-radiative quenching via strong electron-phonon and electron-electron coupling dominates the relaxation processes of the photoexcited state: the PL quantum yield (QY) for bulk Au is reported to be 10^{-10}%.[31] In contrast, the energy gap between the quantized orbitals of Au MPCs exceeds the thermal energy so that they behave like conventional molecules and start to show superior PL properties.[11-22] In this regard, Au MPCs are promising materials with superior and tailored PL properties because their electronic structures can be tuned not only by size but also by shape and composition of the Au core and the nature of the protecting ligands. Their high chemical stability and relatively low cytotoxicity make Au MPCs an attractive tool for medicinal chemistry applications.[32-37] PL emission can be tuned over a wide range, even into the near-infrared (NIR) region, which is important for deep tissue penetration. As a result, Au MPCs are frequently applied as bioimaging agents.[38-41] Recently, Au MPCs have also been used in tumor therapy.[42-44] Au MPCs are actively targeted to cancer cells by surface modification with tumor targeting agents, which are then used to destroy tumor cells via photothermal therapy and reactive oxygen species generated.

In addition, Au MPCs provide us with an ideal opportunity to develop rational design principles of the PL properties for the following reasons: (1) There is an increasing number of Au MPCs whose structures have been determined by single crystal X-ray diffraction (SCXRD) analysis. Such structural information allows us to determine how the PL properties are affected by each structural parameter, (2) the electronic structure of Au MPCs is much simpler than that of other transition metals. The valence

[a] Department of Chemistry, Graduate School of Science, The University of Tokyo, 7-3-1, Hongo, Bunkyo-ku, Tokyo-to, 113-0033, Japan.
[b] Carbon to Metal Coating Institute, Queen's University, Kingston, Ontario, K7L 3N6, Canada.

electrons in Au MPCs are accommodated in discrete orbitals labelled 1S, 1P, 1D, 2S, 2P,… distributed over a jellium-like potential (Figure 1).[45–53] The chemical formula $[Au_xM_y]^z$ (M: ligand) allows us to calculate the formal number of valence electrons (n^*) according to the following equation proposed by Häkkinen:[46]

$$n^* = Ax + By - z \quad (1)$$

where *A* and *B* represent the number of valence electrons supplied by a single metal atom and the ligand M, respectively. Specifically, *A* is 1 for Au, but we should apply suitable *A* values, depending on the group in the periodic table as shown in Table 1 when other elements are doped onto Au MPCs. Meanwhile, *B* is 0 for L-type ligands, such as mono-/diphosphines (PR_3/d-PR_2) and mono-/bis-N-heterocyclic carbenes (NHC/bis-NHC), while it is –1 for X-type ligands, such as halide (X), thiolate (SR), and alkynyl (C≡CR) due to their electron-withdrawing nature.[46] as shown in Table 1.

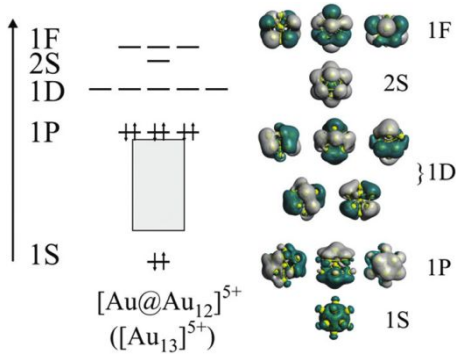

Figure 1. Schematic representation of the electronic structure of Au_{13} MPC including the relevant superatomic orbitals. Reprinted with permission from ref. 37. Copyright 2019 Royal Society of Chemistry.

Table 1. Formal charge state and preferential location of dopant.

Group (element)	Formal charge (A in eq. 1)	Doping location
Group 8 (Ru)	–2	center
Group 9 (Rh, Ir)	–1	center
Group 10 (Ni, Pd, Pt)	0	center
Group 11 (Cu, Ag)	+1	center/surface
Group 12 (Cd, Hg)	+2	surface

The "Au core size" is the primary factor that determines various physicochemical properties of Au MPCs. However, the properties of Au MPCs can also be affected by other parameters such as surface modifications and doping. To understand and highlight the importance of these secondary parameters on the PL properties, this review article focuses on the ubiquitous icosahedral Au_{13} core as a benchmark and addresses the question of how the PL properties are affected by surface modification with ligands (SR,[54–58] C≡CR,[59,60] halogens (X), PR_3/d-PR_2[61,62] or NHC/bis-NHC[63, 64]) and doping of heterometals (Ru, Rh, Ir, Ni, Pd, Pt, Cu, Ag, Cd, Hg).[65–71] Figure 2 shows the geometric structures of the typical examples of Au_{13} MPCs determined by SCXRD: $[Au_{25}(SC_2H_4Ph)_{18}]^-$ (Figure 2a),[72,73] $[Au_{25}(C{\equiv}CPh(CF_3)_2)_{18}]^-$ (Figure 2b),[74] $[Au_{13}(Ph_2PC_2H_4PPh_2)_5Cl_2]^{3+}$ (Figure 2c),[75] and $[Au_{13}(Bzim^{Bn})_9Cl_3]^{2+}$ (Figure 2d).[76] The interfacial structures around the Au_{13} core depend on the type of the ligands. In $[Au_{25}(SC_2H_4Ph)_{18}]^-$ and $[Au_{25}(C{\equiv}CPh(CF_3)_2)_{18}]^-$ protected by X-type ligands, the icosahedral Au_{13} is capped by six bidentate units of $Au_2(SR)_3$ and $Au_2(C{\equiv}CR)_3$, respectively (Figures 2a and 2b).[72–74] In $[Au_{13}(Ph_2PC_2H_4PPh_2)_5Cl_2]^{3+}$ and isostructural $[Au_{13}(bis\text{-}NHC)_5X_2]^{3+}$ protected by L-type ligands, the icosahedral Au_{13} is capped directly by five bidentate phosphines and NHCs, respectively (Figure 2c).[75,77,78] In $[Au_{13}(Bzim^{Bn})_9Cl_3]^{2+}$, the icosahedral Au_{13} is capped directly by nine monodentate NHC ligands and three halides (Figure 2d).[63] Despite the structural diversity in the ligand layers, the n^* values calculated by eq. 1 are 8. According to the theoretical studies, the 1P and 1D superatomic orbitals correspond to the highest occupied molecular orbital (HOMO) and the lowest unoccupied molecular orbital (LUMO) (Figure 1). These Au_{13} MPCs with a closed electron configuration $(1S)^2(1P)^6$ have been considered representative "superatoms".[45–53,72–78] The position of the dopant M in MAu_{12} MPCs depends on the element.[79–92] Group 8–10 elements such as Pd and Pt exclusively occupy the central position (Figure 2e), whereas group 12 elements such as Cd and Hg prefer the surface position (Figure 2f). Nevertheless, the n^* values calculated by eq. 1 are always 8 regardless of the dopants, indicating that MAu_{12} also has a closed electron configuration $(1S)^2(1P)^6$.

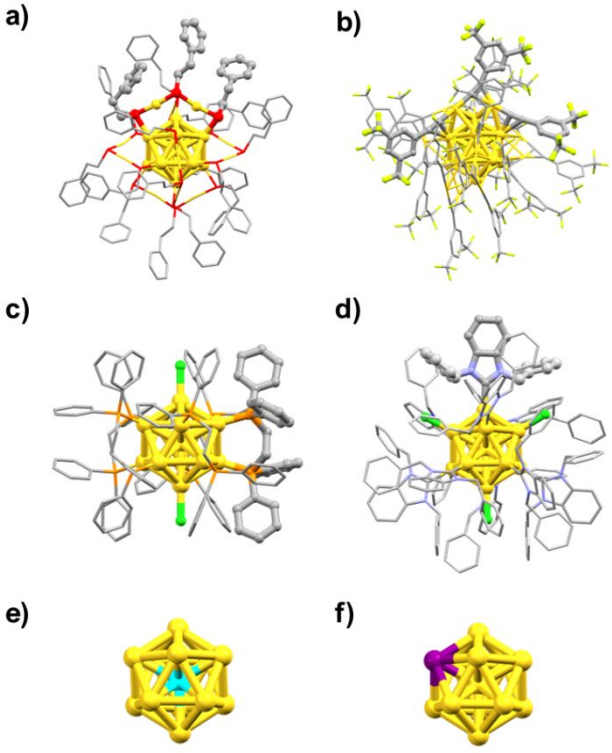

Figure 2. Molecular structures of a) $[Au_{25}(SC_2H_4Ph)_{18}]^-$, b) $[Au_{25}(C{\equiv}CPh(CF_3)_2)_{18}]^-$, c) $[Au_{13}(Ph_2PC_2H_4PPh_2)_5Cl_2]^{3+}$, d) $[Au_{13}(Bzim^{Bn})_9Cl_3]^{2+}$. Color code: Au = yellow, Cl = green, P = orange, N = blue, S = red, F = light green, C = dark grey. Only one ligand each is shown in ball-and-stick representation, other ligands are shown as a wireframe model for improved visualization. Preferential doping site of e) M = Pd, Pt, Rh, Ir, Ru and f) M = Cd, Hg in MAu_{12} core.

The photophysical processes of Au MPCs, like those of conventional fluorophores, can be described as follows. First,

This journal is © The Royal Society of Chemistry 20xx

Please do not adjust margins

the photoexcited state generated by a vertical transition from the ground state (S_0) relaxes to the vibrational ground state of the first electronically excited state (S_1) according to Kasha's rule. Then, three relaxation pathways compete: (1) non-radiative internal conversion (IC) to the vibrational excited state of S_0, (2) radiative decay to the vibrational states in the Franck-Condon region in the S_0 state (fluorescence), (3) intersystem crossing (ISC) to the triplet state (T_1) followed by radiative decay (phosphorescence) to the S_0 state.[93–95] In the presence of other molecules, deactivation of the T_1 state can occur via energy transfer (ET) to oxygen or emitter molecules, followed by generation of singlet oxygen[96–98] or upconverted fluorescence emission,[99] respectively. Another deactivation pathway for photoexcited Au MPC is via electron transfer (eT), which can be applied to photoredox catalysis.[91,100,101] In most cases, the radiative decay of small Au MPCs is dominated by phosphorescence rather than fluorescence due to the strong spin-orbit coupling due to the heavy atom effect. However, in contrast to the case of conventional organic emitters, the radiative decay mechanism of Au MPCs cannot be distinguished by the PL lifetime alone due to the fast ISC and vibrational quenching, resulting in phosphorescence lifetimes of Au MPCs in the range of 100 ns. Therefore, additional experimental evidence (*e.g.* by triplet state quenching or transient absorption spectroscopy) is required. An overview of the emission mechanisms in Au MPCs was recently provided by Jin.[22]

Emission energy (E_{em}) and QY are the key PL properties of Au MPCs that should be tuned for the application. In general, the E_{em} reflects the electronic structures of Au NCs, such as the energy gap (E_{HL}) between HOMO and LUMO. The E_{em} is also affected by the relaxation in the electronically excited states, which is determined by the potential energy curves in the S_1 and T_1 states. The PLQY, on the other hand, is also related to the E_{HL} according to the energy gap law: the rate of non-radiative IC quenching increases inversely proportional to the E_{HL}.[102,103] Similarly, the luminescence lifetime follows the energy gap law, and increasing the E_{HL} usually leads to elongated PL lifetimes. Therefore, the E_{HL} is a primary descriptor to characterize the PL properties. In other words, the PL properties can be tuned by controlling the E_{HL}.

In this review article, we first show that the E_{HL} values of Au_{13}/MAu_{12} MPCs reported so far are distributed over a wide range of 1.2–2.3 eV, although they all share a common electron configuration of $(1S)^2(1P)^6$. These data indicate that the electronic structures of Au_{13} MPC can be finely tuned by the choice of protecting ligands and the dopants. Then, we summarize the PL properties (E_{em} and PLQY) of Au_{13}/MAu_{12} MPCs and extract empirical rules on how to tune the E_{em} values and to enhance the PLQY by the surface modification and doping. In addition, we attempted to rationalize these empirical rules based on modified spherical jellium models. Finally, we discuss the challenges for the future development of Au-based MPCs with designed PL properties. We hope that this review article will help the audience to establish the rational guidelines for designed PL properties.

2. Ligand Effects

This section will showcase the characteristic PL properties of Au_{13} MPCs protected by the respective ligands. Figures 3 and 4 plot the E_{em} and PLQY values as a function of E_{HL}, respectively. The data points for Au_{13} MPCs are indicated by different colors depending on the ligands: thiolates (blue), selenolate (purple), alkynyls (green), phosphines (red), and N-heterocyclic carbenes (orange). The E_{HL} was determined either by the onset in the optical absorption spectrum or by a voltametric method, while the E_{em} was determined by the peak position in the PL spectrum. Thus, the estimated optical E_{HL} values tend to underestimate the true values. All data presented were recorded under ambient atmosphere unless otherwise noted. In the following, the ligands are divided into two categories, X-type and L-type ligands.

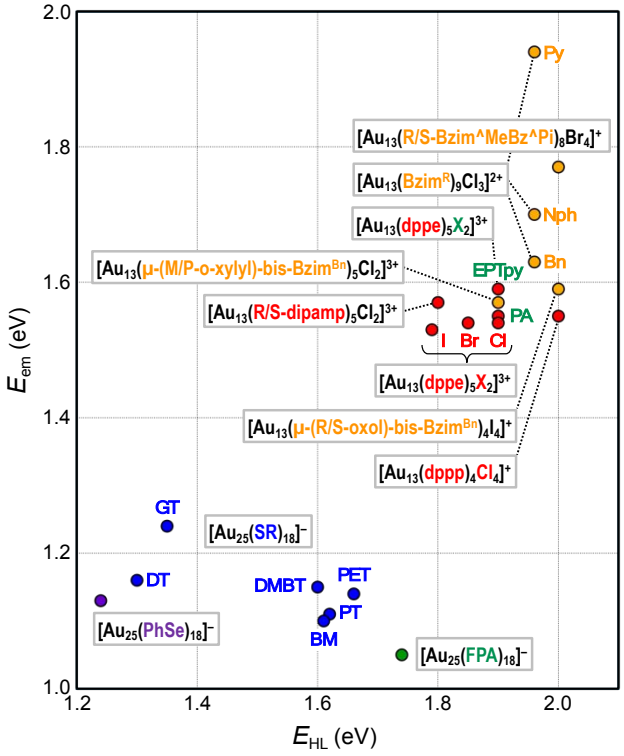

Figure 3. Overview of E_{em} as a function of E_{HL} for Au_{13} MPCs. Color code: thiolate (blue), selenolate (purple), alkynyl (green), phosphine (red), NHC (orange).

2.1. X-type Ligands

2.1.1. Thiolates

The E_{HL} and E_{em} values of Au_{13} protected by various thiolates (RS, Scheme 1) are in the range of 1.30–1.66 and 1.10–1.24 eV, respectively, depending on the structure of the R group (blue dots in Figure 3). The PLQY was relatively small and distributed in the range of 0.1–1.7% (blue dots in Figure 4). More detailed descriptions of the effects of the thiolate structure on the PL properties are given below.

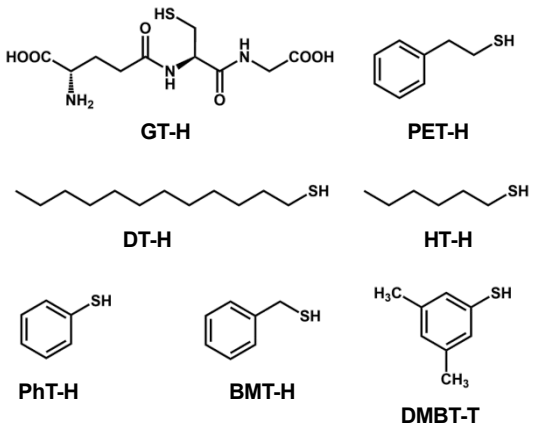

Scheme 1. Structures and abbreviations of the RS ligands used to protect the Au_{13} core in Section 2.1.1.

$[Au_{25}(GT)_{18}]^-$ (GT-H = glutathione, Scheme 1): This cluster is the first member of the ubiquitous family of $Au_{25}(SR)_{18}$, reported by Negishi and Tsukuda in 2005.[104,105] The E_{HL} and E_{em} were 1.35 and 1.24 eV,[94] respectively (Figure 3), while the PLQY was only $2x10^{-3}$% (Figure 4). The PL intensity of $[Au_{25}(GT)_{18}]^-$ was increased by ~1.8 times in $[Au_{25}(GT)_{18-x}(SPNA)_x]^-$, where PNA represents a long-chain peptide nucleic acid with a high proportion of electron-rich N and O atoms.[106] This enhancement was attributed to electron donation by electron-rich groups of SPNA (*e.g.* carboxy and amino groups) to the Au_{13} core.

$[Au_{25}(PET)_{18}]^-$ (PET-H = phenylethylthiol, Scheme 1): This cluster is the first member of the $Au_{25}(SR)_{18}$ family whose structures were theoretically predicted by Grönbeck,[107] and experimentally determined independently by Murray[72] and Jin[73] in 2008. The E_{HL} and E_{em} were 1.66 and 1.14 eV, respectively, indicating a large Stokes shift (Figure 3).[108] Note that this E_{HL} corresponds to the value at 0 K estimated from temperature-dependent optical spectra based on the Bose-Einstein model and is larger than that estimated from optical onset.[104] The PLQY was only $1x10^{-2}$% (Figure 4).[106] $[Au_{25}(PET)_{18}]^-$ showed a fluorescence lifetime of 0.73 μs. Theoretical calculations by Aikens revealed that the PL is dominated by core-based transitions with a very small contribution from the outer Au atoms in the staple ligands.[109]

$[Au_{25}(DT)_{18}]^-$ and **$[Au_{25}(HT)_{18}]^-$** (DT-H = 1-dodecanethiol; HT-H = 1-hexanethiol, Scheme 1): The E_{HL} and E_{em} of $[Au_{25}(DT)_{18}]^-$ were 1.3 and 1.16 eV, respectively (Figure 3).[110, 111] Wu and Jin reported that the PLQYs of $[Au_{25}(DT)_{18}]^-$ and $[Au_{25}(HT)_{18}]^-$ were $5x10^{-3}$ and $2x10^{-3}$%, respectively (Figure 4).[106] The PLQY of $[Au_{25}(SR)_{18}]^-$ decreased in the order of SR = PET > DT > HT, which is parallel to the order of the ability of the ligands to donate electronic charge to the Au_{13} core. The PL lifetimes were 0.42 and 0.64 μs for $[Au_{25}(DT)_{18}]^-$ and $[Au_{25}(HT)_{18}]^-$, respectively. Theoretical calculations revealed that core-based transitions as well as ligand-core interactions are essential for the PL behavior of $[Au_{25}(SR)_{18}]^-$ (R = H, CH_3, C_2H_5, C_3H_7).[109]

$[Au_{25}(PhT)_{18}]^-$, **$[Au_{25}(BMT)_{18}]^-$**, **$[Au_{25}(DMBT)_{18}]^-$** (PhT-H = phenylthiol, BMT-H = benzylmethanethiol, DMBT-H = 3,5-dimethylbenzenethiol, Scheme 1): Effects of aromatic thiolates on the optical properties of $[Au_{25}(SR)_{18}]^-$ have been reported by Jin.[108] The E_{HL} and E_{em} of $[Au_{25}(SR)_{18}]^-$ (SR = PhT, BMT, DMBT) were comparable to those of $[Au_{25}(PET)_{18}]^-$ (Figure 3), indicating that the aromatic group does not significantly affect the electronic structures. $[Au_{25}(SR)_{18}]^-$ (SR = PhT, BMT, DMBT) showed PLQYs of 1.7, 1.5 and 1.3%, respectively (Figure 4), significantly larger than that of $[Au_{25}(PET)_{18}]^-$.

Typically, $[Au_{25}(SR)_{18}]^-$ exhibits an E_{em} in the NIR region and PLQYs of <2%. Overall, the geometric structure of the R group does not significantly affect the electronic structures of $[Au_{25}(SR)_{18}]^-$ in terms of the E_{HL} and E_{em}, because the HOMO and LUMO are mostly localized in the common Au_{13} cores. In contrast, the electronic structure of the R group affects the PLQYs. In particular, R groups with electron-rich atoms (*e.g.*, O, N) or functional groups enhance the PLQY by donating electronic charge to the Au_{13} core.

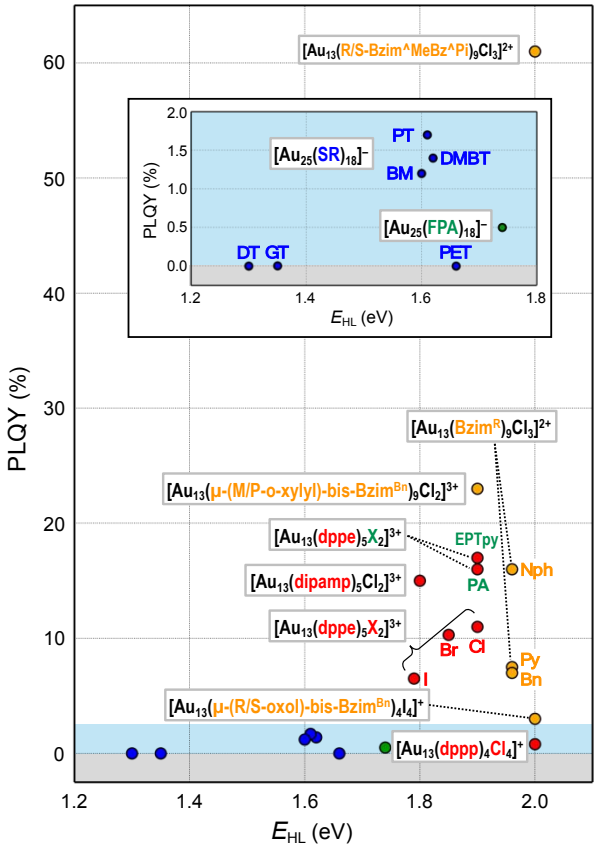

Figure 4. Overview of PLQYs as a function of E_{HL} for Au_{13} MPCs protected by X-type ligands (inset) and L-type ligands. Color code: thiolate (blue), alkynyl (green), phosphine (red), NHC (orange).

2.1.2. Selenolates

$[Au_{25}(PhSe)_{18}]^-$ (PhSe-H = phenylselenol): PhSe, an analogue of PhS, was used by the group of Wu to protect the Au_{13} core.[112] Square-wave voltammetry of $[Au_{25}(PhSe)_{18}]^-$ revealed a E_{HL} of 1.24 eV, which is significantly smaller than that for $[Au_{25}(PhT)_{18}]^-$ (1.6 eV). The E_{em} of $[Au_{25}(PhSe)_{18}]^-$ was 1.13 eV (purple dot in Figure 3), comparable to that of $[Au_{25}(PET)_{18}]^-$ (1.14 eV), while the PLQY was not reported.

2.1.3. Alkynyls

The molecular structures of the alkynyls used are shown in Scheme 2.

This journal is © The Royal Society of Chemistry 20xx

Please do not adjust margins

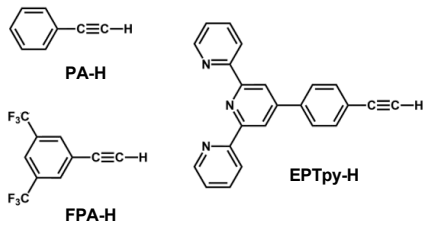

Scheme 2. Structures and abbreviations of the alkynyl ligands used to protect the Au_{13} core in Sections 2.1.3 and 2.2.1.

$[Au_{25}(FPA)_{18}]^-$ (FPA-H = 3,5-bis(trifluoromethyl)phenylacetylene, Scheme 2): Wang synthesized $[Au_{25}(FPA)_{18}]^-$ by direct reduction of the precursor gold complex Au(I)-FPA.[74] While the Au(I)-alkynyl staples have similar structures to Au(I)-SR staples (Figure 2b), $[Au_{25}(FPA)_{18}]^-$ has a chiral D_3 symmetry, due to the higher steric demand of alkynyl ligands than thiolates in $[Au_{25}(SR)_{18}]^-$. The E_{HL} and E_{em} of $[Au_{25}(FPA)_{18}]^-$ were 1.74 (determined electrochemically) and 1.05 eV, respectively (green dot in Figure 3).[87] The PLQY was 0.5% (green dot in Figure 4).

2.2. L-type Ligands

In contrast to the formation of short staple motifs in the protection by X-type ligands (Figures 2a and 2b), L-type ligands such as phosphines and N-heterocyclic carbenes bind directly to the Au_{13} core together with auxiliary X-type ligands (Figures 2c and 2d).

2.2.1. Phosphines

With few exceptions such as $[Au_{13}(PPhMe_2)_{10}Cl_2]^{3+}$,[113] $[Au_{13}(PPh_2Me)_8Cl_4]^+$,[114] and $[Au_{13}(P(Oct)_3)_8Cl_4]^+$,[115] diphosphines (Scheme 3) have been conventionally used as protecting ligands of Au_{13}. The E_{HL} and E_{em} values of diphosphine-protected Au_{13} are in the range of 1.79–1.90 and 1.53–1.57 eV, respectively (red dots in Figure 3). The PLQY was in the range of 6–17% (red dots in Figure 4), which is significantly larger than those of Au_{13} protected by X-type ligands (section 2.1). This section focuses on the effects of diphosphine structures (Scheme 3) on the PL properties.

$[Au_{13}(dppe)_5X_2]^{3+}$ (dppe = 1,2-bis(diphenylphosphino)ethane, X = Cl, Br, I, Scheme 3): $[Au_{13}(dppe)_5Cl_2]^{3+}$ was synthesized by Konishi in 2010 using size focusing ("etching") with HCl.[75] The E_{HL} and E_{em} were 1.9 and 1.55 eV, respectively (red dots in Figure 3). The PLQY was 11% (red dot in Figure 4) with a phosphorescence lifetime of 2.69 μs.[116] The E_{HL} of $[Au_{13}(dppe)_5X_2]^{3+}$ decreased in the order of X = Cl > Br > I from 1.90 to 1.79 eV, while the E_{em} values were comparable (1.53–1.54 eV) regardless of X.[117] Accordingly, the PLQY decreased in the same order by 11% (Cl) > 10.3% (Br) > 6.5% (I) (red dots in Figure 4).

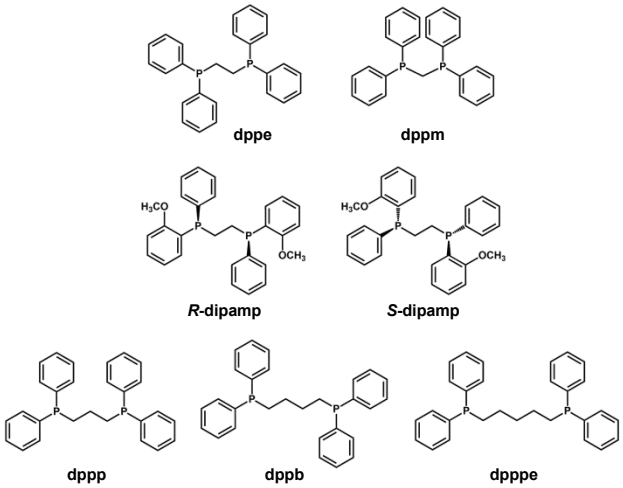

Scheme 3. Structures and abbreviations of the diphosphine ligands used to protect the Au_{13} core in Section 2.2.1.

$[Au_{13}(dppe)_5(PA)_2]^{3+}$ (PA-H = phenylacetylene, Scheme 2): Konishi synthesized $[Au_{13}(dppe)_5(PA)_2]^{3+}$ via a ligand exchange reaction of $[Au_{13}(dppe)_5Cl_2](PF_6)_3$ with PA-H.[116] The E_{HL} of $[Au_{13}(dppe)_5(PA)_2]^{3+}$ (1.9 eV) was same as that of $[Au_{13}(dppe)_5Cl_2]^+$ (red dot in Figure 3). DFT calculations showed that the HOMO of $[Au_{13}(dppe)_5(PA)_2]^{3+}$ is extended over the PA units. Likewise, HOMO–1, HOMO–2 and HOMO–3 with superatomic P-like character located on the Au_{13} core are distributed over the π system of PA. The interaction of the superatomic valence electrons of Au_{13} with the π-orbitals then leads to the generation of new and unique molecular orbitals. The E_{em} value of $[Au_{13}(dppe)_5(PA)_2]^{3+}$ (1.55 eV, red dot in Figure 3) was also comparable to that of $[Au_{13}(dppe)_5Cl_2]^+$, the PLQY of the former (16%, red dot in Figure 4) was higher than that of the latter (11%), which has attributed to a higher quenching effect of Cl in comparison to PA. This trend is consistent with the longer PL lifetime of the former (3.51 μs) compared to the latter (2.69 μs).

$[Au_{13}(dppe)_5(EPTpy)_2]^{3+}$ (EPTpy-H = 4'-(4-ethynylphenyl)-2,2':6',2''-terpyridine, Scheme 2): In 2023, our group successfully obtained $[Au_{13}(dppe)_5(EPTpy)_2]^{3+}$ with two terpyridyl moieties on opposite sides of the Au_{13} core.[118] The E_{HL}, E_{em} and PLQY of $[Au_{13}(dppe)_5(EPTpy)_2]^{3+}$ (1.9 eV, 1.59 eV, 17%) were comparable to those of $[Au_{13}(dppe)_5(PA)_2]^{3+}$ (1.9 eV, 1.55 eV, 16%). The PL of $[Au_{13}(dppe)_5(EPTpy)_2]^{3+}$ was completely quenched by coordination of Co^{2+}, Ni^{2+} or Cu^{2+} at the terpyridyl moieties, but not by Zn^{2+}.[118] The PL lifetime of $[Au_{13}(dppe)_5(EPTpy)_2]^{3+}$ decreased from 3.66 μs to 0.02 μs upon coordination of Co^{2+}, while it remained unchanged upon coordination of Zn^{2+} (3.41 μs). This PL quenching phenomenon was explained by efficient energy transfer from the photoexcited Au_{13} core to the d^9 transition metal cations via electron exchange between them.

$[Au_{13}(R/S\text{-dipamp})_5Cl_2]^{3+}$ (*R*/*S*-dipamp = (*R*,*R*)/(*S*,*S*)-2-bis[(2-methoxyphenyl)phenylphosphino]ethane, Scheme 3): Yang reported the synthesis of enantiopure Au_{13} clusters $[Au_{13}(R\text{-dipamp})_5Cl_2]^{3+}$ and $[Au_{13}(S\text{-dipamp})_5Cl_2]^{3+}$ using the chiral diphosphine *R*/*S*-dipamp.[119] The E_{HL} of $[Au_{13}(R\text{-dipamp})_5Cl_2]^{3+}$ (1.8 eV) was slightly smaller than that of $[Au_{13}(dppe)_5Cl_2]^{3+}$ (1.9 eV) (red dots in Figure 3). Konishi showed that the E_{em} of $[Au_{13}(R\text{-dipamp})_5Cl_2]^{3+}$ (1.57 eV) was comparable to that of $[Au_{13}(dppe)_5Cl_2]^{3+}$ (1.54 eV) (red dots in Figure 3) and that the PLQY (15%) was slightly higher than that of $[Au_{13}(dppe)_5Cl_2]^{3+}$ (11%) (red dots in Figure 4).[120] This was attributed to an increased core rigidification, as the chiral *R*/*S*-dipamp ligands induced additional torsional strain on the icosahedral Au core. $[Au_{13}(R\text{-dipamp})_5Cl_2]^{3+}$ and $[Au_{13}(S\text{-dipamp})_5Cl_2]^{3+}$ exhibited circularly polarized luminescence (CPL) with emission maxima at 1.63 eV and emission anisotropy factors of 2.5×10^{-3} and 2.3×10^{-3}, respectively.[120]

$[Au_{13}L_4Cl_4]^+$ (L = $Ph_2P–(CH_2)_m–PPh_2$ with *m* = 3 (dppp), 4 (dppb), 5 (dpppe), Scheme 3): The chemical formula of Au_{13} protected by long

Please do not adjust margins

bis(diphenylphosphino) ligands $[Au_{13}L_4Cl_4]^+$ (m = 3 – 5) differ from $[Au_{13}(dppe)_5Cl_2]^{3+}$ (m = 2).[115] Konishi reasonably proposed that $[Au_{13}L_4Cl_4]^+$ adapted an icosahedral Au_{13} core, although SCXRD analysis was not possible. The absorption spectrum profiles of $[Au_{13}L_4Cl_4]^+$ (m = 3 – 5) were similar regardless of m, but were significantly different from that of $[Au_{13}(dppe)_5Cl_2]^{3+}$ (m = 2). While the E_{HL} and E_{em} values of $[Au_{13}(dppp)_4Cl_4]^+$ (~2.0 and 1.60 eV, red dots in Figure 3) were similar to those of $[Au_{13}(dppe)_5Cl_2]^{3+}$ (~2.0 and 1.55 eV, red dots in Figure 4), the PLQY of $[Au_{13}(dppp)_4Cl_4]^+$ (0.8%) was significantly lower than that of $[Au_{13}(dppe)_5Cl_2]^{3+}$ (11%). This remarkable PL quenching suggests that diphosphines linked by longer alkyl chains cannot rigidify the Au_{13} and thus cannot suppress non-radiative decay. The PL properties of $[Au_{13}L_4Cl_4]^+$ (m = 4, 5) have not been reported.

Overall, the E_{HL} and E_{em} values of diphosphine-protected Au_{13} are larger than those of Au_{13} protected by X-type ligands as shown in section 2.1. The PLQYs were significantly increased compared to those of thiolate-protected Au_{13}. This trend is in parallel to the energy gap law between PLQY and E_{HL}.[102,103] The mechanical stress imposed by the bidentate ligation of diphosphines may contribute to the suppression of non-radiative decay by stiffening the Au_{13} core and to the emerge of CPL by distorting the Au_{13} core into a chiral structure. Alkynyls as X-type auxiliary ligands largely enhance the E_{HL} by electronic conjugation, while the effect of halides as X-type auxiliary ligands is relatively small.

2.2.2. Arsines and Stibines

In contrast to monodentate phosphines, monodentate arsines and stibines can protect the icosahedral Au_{13} core.

$[Au_{13}(AsPh_3)_8Cl_4]^+$: The $[Au_{13}(AsPh_3)_8Cl_4]^+$ reported by Sun exhibited a phosphorescence of E_{em} = 1.55 eV,[121] which is comparable to that of $[Au_{13}(dppe)_5Cl_2]^{3+}$ (1.54 eV), but smaller than that of $[Au_{13}(P(Oct)_3)_8Cl_4]^+$ (E_{em} = 1.60 eV).[115] No other PL properties, including the PL QY, have been reported.

$[Au_{13}(dpap)_5Cl_2]^{3+}$ (dpap = $Ph_2As–(CH_2)_3–AsPh_2$): Konishi reported on the diarsine-protected cluster $[Au_{13}(dpap)_5Cl_2]^{3+}$.[122] The E_{HL} was ~2.0 eV, while the E_{em} and PLQY were 1.63 eV and 7%, respectively. The E_{em} and PLQY were slightly larger and smaller than those of $[Au_{13}(dppe)_5Cl_2]^{3+}$ (1.55 eV and 11%, respectively). The difference in their electronic structures was attributed to subtle deformation of the Au_{13} icosahedron, rather than the coordinating atoms (As or P).

$[Au_{13}L_8Cl_4]^+$ (L = $SbPh_3$, Sb(p-tolyl)$_3$): Leong reported that $[Au_{13}L_8Cl_4]^+$ exhibited both fluorescence at E_{em} = 1.68 eV and phosphorescence at E_{em} = 1.50 eV due to a heavy metal effect of Sb.[123] This dual emission behavior of $[Au_{13}L_8Cl_4]^+$ was attributed to facilitated reverse ISC from the T_1 to the S_1 state.

Overall, the E_{em} values for the phosphorescence increase in the order of $[Au_{13}(SbPh_3)_8Cl_4]^+$ < $[Au_{13}(AsPh_3)_8Cl_4]^+$ < $[Au_{13}(P(Oct)_3)_8Cl_4]^+$.

2.2.3. N-Heterocyclic Carbenes

In contrast to the phosphine ligands, NHC ligands can stabilize the Au_{13} cores even in monodentate form via strong Au–C bonds.[124] Further stabilization can be achieved by using bidentate NHC ligands. One of the practical advantages of NHCs is their structural designability for fine-tuning the PL properties of Au_{13} NCs. Therefore, the effects of the substituent group R at the wingtips and multidentate ligation on the PL properties have been systematically investigated. The molecular structures of the NHCs used are shown in Scheme 4. The E_{HL} values of NHC-protected Au_{13} are nearly constant at ~2.0 eV, while the E_{em} values vary over a wide range of 1.57–1.94 eV (orange dots in Figure 3). The PLQYs are comparable to those of diphosphine-protected Au_{13} in most cases, but it can be as high as 61% when using a specific NHC (orange dots in Figure 4). The increase in PLQY was attributed to the stiffening of the Au_{13} core by π···π or C–H···π interaction between the adjacent NHC ligands. More detailed descriptions of the effects of the NHC structures on the PL properties are given below.

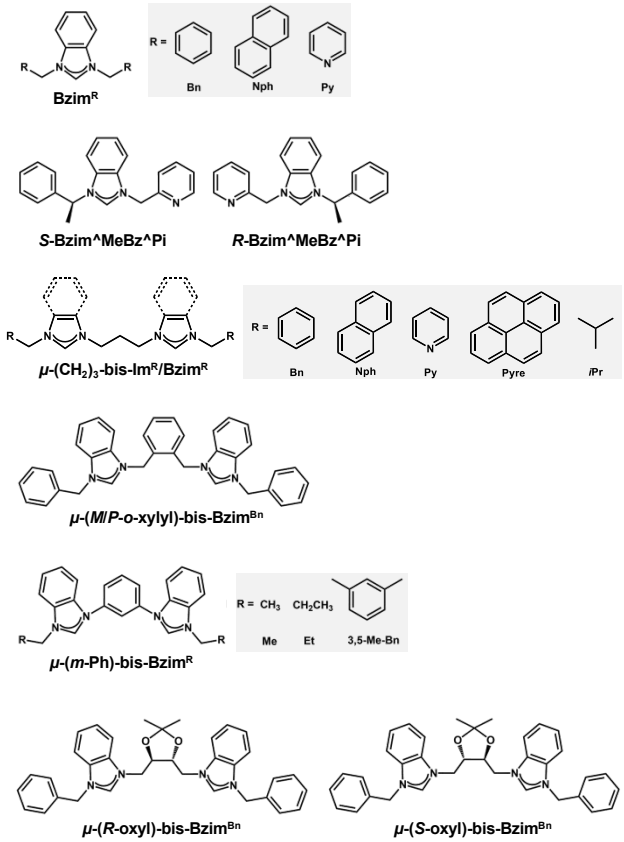

Scheme 4. Structures and abbreviations of the NHC ligands used to protect the Au_{13} core in Section 2.2.3.

$[Au_{13}(Bzim^R)_9Cl_3]^{2+}$ ($Bzim^R$ = benzyl/naphthyl/pyridyl-benzimidazole for R = Bn, Nph, and Py, respectively, Scheme 4): $[Au_{13}(Bzim^R)_9Cl_3]^{2+}$ is an ideal benchmark system to study how the wingtips of NHC ligands affect the PL properties.[76,77] While the E_{HL} values were ~2.0 eV independent of R, the E_{em} values were 1.63, 1.70 and 1.94 eV (orange dots in Figure 3) with the PLQYs of 7, 16, and 7.5% (orange dots in Figure 4), for R = Bn, Nph, and Py, respectively. The highest PLQY for R = NPh was explained by the stiffening of the Au_{13} core by the π···π interaction between the naphthyl wingtips.

$[Au_{13}(R/S\text{-Bzim^MeBz^Pi})_8Br_4]^+$ (R/S-Bzim^MeBz^Pi = R/S-pyridine-ylmethylbenzylbenzimidazole, Scheme 4): Zang reported the synthesis of enantiopure Au_{13} clusters $[Au_{13}(R\text{-Bzim^MeBz^Pi})_8Br_4]^+$ and $[Au_{13}(S\text{-Bzim^MeBz^Pi})_8Br_4]^+$ using chiral benzimidazole ligands.[125] The E_{HL} and E_{em} values were 2.00 and

This journal is © The Royal Society of Chemistry 20xx

Please do not adjust margins

1.77 eV, respectively (orange dot in Figure 3). The PLQY was as high as 61% (orange dot in Figure 4) with a PL lifetime of 3.07 μs. This extraordinary high PLQY was explained by the combination of two factors: rigidification of the Au_{13} core by multiple interligand interactions such as C–H···N, C–H···π, C–H···Au and π···π interactions and higher electron-donating capability of *R*/*S*-Bzim^MeBz^Pi than other NHC ligands. $[Au_{13}(R\text{-Bzim^MeBz^Pi})_8Br_4]^+$ and $[Au_{13}(S\text{-Bzim^MeBz^Pi})_8Br_4]^+$ exhibited CPL with the E_{em} of 1.63 eV and a dissymmetry factor of 2.65×10^{-3} in a frozen DCM solution.

$[Au_{13}(\mu\text{-}(CH_2)_3\text{-bis-Bzim}^R)_5X_2]^{3+}$ (μ-$(CH_2)_3$-bis-$Bzim^R$ = μ-propyl-di-benzyl/naphthyl/pyridyl/pyrenyl-bisbenzimidazole for R = Bn, Nph, Py, Pyre; X = Cl, Br, Scheme 4): Although the PL properties of these MPCs could not be plotted in Figures 3 and 4 due to the lack of the E_{HL} values, the remarkable effects of the wingtips on the PL were observed. The E_{em} values of $[Au_{13}(\mu\text{-}(CH_2)_3\text{-bis-Bzim}^{Bn})_5Br_2]^{3+}$ and $[Au_{13}(\mu\text{-}(CH_2)_3\text{-bis-Bzim}^{Py})_5Br_2]^{3+}$ were 1.91 and 1.94 eV, respectively, while their PLQYs were both 15%.[126] Extending the π-conjugation of the R group further improved the PLQY. The PLQY increased from 38% for $[Au_{13}(\mu\text{-}(CH_2)_3\text{-bis-Bzim}^{Nph})_5Cl_2]^{3+}$ to 56% for $[Au_{13}(\mu\text{-}(CH_2)_3\text{-bis-Bzim}^{Pyre})_5Cl_2]^{3+}$, while their E_{em} values were both 1.75 eV. Consistent with this enhancement of the PLQY, their PL lifetimes were extended from 2.6 to 3.4 μs. This enhancement of the PLQY is associated with the stiffening of the Au_{13} core by stronger π···π interaction between the adjacent ligands. The PLQYs of $[Au_{13}(\mu\text{-}(CH_2)_3\text{-bis-Bzim}^R)_5X_2]^{3+}$ were higher than those of $[Au_{13}(Bzim^{Bn})_9Cl_3]^{2+}$ (7%).[77,126] This enhancement of PLQY was attributed to the suppression of non-radiative decay of the photoexcited state by restricting the motion of the Au_{13} core by the bidentate coordination of μ-$(CH_2)_3$-bis-$Bzim^R$.

$[Au_{13}(\mu\text{-}(CH_2)_3\text{-bis-Im}^R/Bzim^R)_m(tpp)_nX_2]^{3+}$ (μ-$(CH_2)_3$-bis-Im^R = μ-propyl-di-benzyl/*iso*-propyl-bis(benz)imidazole for R = Bn, *i*Pr; tpp = PPh_3; X = Cl, Br; (*m*, *n*) = (2, 4), (3, 3), Scheme 4): The Biffis group reported mixed NHC/phosphine protected Au_{13} clusters.[127] All clusters showed the same E_{em} of 1.63 eV regardless of R or NHC/phosphine ratio, while the E_{HL} of the clusters was not reported. The PLQYs were significantly different depending on the NHC/phosphine ratio. $[Au_{13}(\mu\text{-}(CH_2)_3\text{-bis-Im}^{Bn})_2(tpp)_4Cl_2]^{3+}$ and $[Au_{13}(\mu\text{-}(CH_2)_3\text{-bis-Bzim}^{Bn})_2(tpp)_4Cl_2]^{3+}$ and showed QYs of 4 and 3%, respectively, while $[Au_{13}(\mu\text{-}(CH_2)_3\text{-bis-Bzim}^{Bn})_3(tpp)_3Cl_2]^{3+}$ showed a high PLQY of 44%. This was attributed to increased rigidity due to a higher number of NHC ligands. PL lifetimes of the clusters were not reported.

$[Au_{13}(\mu\text{-}(M/P\text{-}o\text{-xylyl})\text{-bis-Bzim}^{Bn})_5Cl_2]^{3+}$ (μ-(*M*/*P*-*o*-xylyl)-bis-$Bzim^{Bn}$ = minus/plus-(μ-*o*-xylyl)-dibenzyl-bisbenzimidazole, Scheme 4): The E_{HL} and E_{em} of $[Au_{13}(\mu\text{-}(M/P\text{-}o\text{-xylyl})\text{-bis-Bzim}^{Bn})_5Cl_2]^{3+}$ were 1.9 and 1.57 eV, respectively (orange dot in Figure 3).[78] The PLQY was 23% (orange dot in Figure 4), which is higher than that of the monodentate counterpart $[Au_{13}(Bzim^{Bn})_9Cl_3]^{2+}$ (7%). This led to an increased core rigidification due to both bidentate coordination by the ligand system on the one hand, and the exertion of torsional strain on the Au core on the other hand. These effects prevented vibrational quenching of the excited state. Although CPL properties might be expected due to the ligand-induced torsion of the Au_{13} core, CPL spectra have not been reported.

$[Au_{13}(\mu\text{-}(m\text{-Ph})\text{-bis-Bzim}^R)_5Br_2]^{3+}$ (μ-(*m*-Ph)-bis-$Bzim^R$ = μ-(*m*-phenylene)-di-methyl/ethyl/3,5-dimethylbenzyl-bis-benzimidazole for R = Me, Et, 3,5-Me_2Bn, Scheme 4): $[Au_{13}(\mu\text{-}(m\text{-Ph})\text{-bis-Bzim}^R)_5Br_2]^{3+}$, reported by Mak, demonstrated the key role of the NHC wingtip R in the relaxation behavior of bis-NHC Au_{13}.[128] While the E_{em} value was nearly constant (1.75 eV) regardless of R, the PLQYs increased from 8 to 16% in the order of R = Me < Et < 3,5-Me_2Bn, which was explained by an increased rigidification by the bulkier ligand systems. Counterintuitively, the PL lifetime decreased from 1.03 to 0.80 μs in the same order. The origin of the discrepancy between the PLQY and the PL lifetime is unknown.

$[Au_{13}(\mu\text{-}(R/S\text{-oxol})\text{-bis-Bzim}^{Bn})_4I_4]^+$ (μ-(*R*/*S*-oxol)-bis-$Bzim^{Bn}$ = μ-(*R*/*S*-2,2-dimethyl-1,3-dioxolane)-dibenzyl-bis-benzimidazole, Scheme 4): The number of bis-NHC ligands (4) in this cluster is smaller than that in other Au_{13} NCs protected by bis-NHC ligands (5) due to the greater steric hindrance of the ligands.[129] $[Au_{13}(\mu\text{-}(R/S\text{-oxol})\text{-bis-Bzim}^{Bn})_4I_4]^+$ showed an E_{HL} of 2.0 eV and an E_{em} of 1.59 eV (orange dot in Figure 3). The PLQY was 3% (orange dot in Figure 4), which is significantly lower compared to the bis-NHC stabilized Au_{13} NCs mentioned above. This behavior was attributed to less efficient core stiffening due to a smaller number of NHC ligands and confinement of valence electrons to a smaller volume due to a larger number of X-type ligands.

2.3. Qualitative Explanation of Ligand Effects on the PL Properties

Overall, Figure 3 shows that E_{HL} values of the Au_{13} core can be tuned over a wide range of 1.2–2.0 eV by surface modification. There is a clear trend that E_{HL} values for the Au_{13} NCs protected by L-type ligands (phosphines, NHCs) are much larger than those by X-type ligands (thiolates, alkynyls). We previously explained this trend based on the spherical jellium model (Figure 5). The Au_{13} protected by X-type ligands is viewed as a formal Au_{13}^{5+} core protected by six electronegative surface units (e.g. $[Au_2(SR)_3]^-$). In contrast, the Au_{13} protected by L-type ligands is viewed as a formal Au_{13}^{5+} core protected by mostly by electroneutral ligands with few electronegative ligands (e.g. halogen, alkynyls). We make a simple assumption that the isotropic siege of the Au_{13} core by electroneutral ligands leads to the expansion of potential volume for the confinement of valence electrons (step ❶ in Figure 5), and thereby stabilizing both HOMO and LUMO orbitals, corresponding to 1P and 1D superatomic orbitals, respectively (step ❷ in Figure 5). If we assume that the 1P orbitals have a lager populated outer region of the core than the 1D orbitals, we can predict that the 1P orbitals are stabilized more than 1D orbitals when reducing the negative charge on the ligand layer by using L-type ligands.[53] This qualitatively explains why the E_{HL} values of Au_{13} protected by L-type ligands are obviously larger than those of Au_{13} protected by X-type ligands.

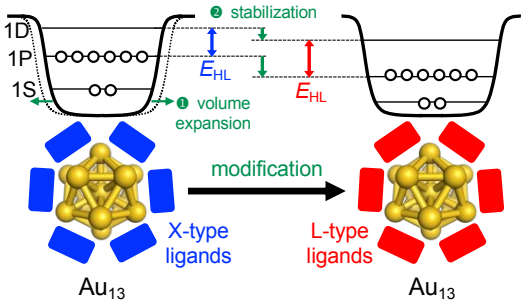

Figure 5. Schematic jellium potentials for the Au_{13}(8e) core protected by X-type (left) and L-type (right) ligands. The blue and red rectangles represent X-type and L-type ligands, respectively.

Figure 3 shows that the E_{em} values for the Au_{13} NCs protected by L-type ligands (1.5–1.9 eV) are much larger than those by X-type ligands (1.1–1.3 eV). This ligand effect is not only due to larger E_{HL} values for the former, but also smaller Stokes shift for the L-type ligation (0–0.4 eV) than X-type ligation (0.1–0.6 eV). The trend in the Stokes shift suggests that the photoexcited state of Au_{13} NC protected by X-type ligands undergoes larger relaxation, but the reason is not clear at this moment.

Figure 4 illustrates that the PLQYs for the protection with L-type ligands are much larger than those with X-type ligands. The PL of Au_{13} protected by L-type ligands is basically assigned to phosphorescence from T_1 state because the excited lifetime is in the order of μs.[95] The correlation between the E_{HL} and PLQY is in line with the energy gap law in which an expansion of the E_{HL} can efficiently suppress the non-radiative decay process of photoexcited states.[102,103] Practically, L-type ligands are suitable to enhance the PLQY. Further enhancement in PLQY is expected by proper design of the ligand structures to enhance the noncovalent interaction (π···π, C–H···π, and hydrogen bonding) between the adjacent ligands. The nonradiative decay of the photoexcited state can be suppressed by the rigidification of the Au_{13} core by these interligand interactions. Recently, Tsukuda demonstrated the importance of ligand packing on the PLQY. The PLQY of $[IrAu_{12}(dppe)_5(PA)_2]^+$ decreased from 53% to 25% upon the removal of one PA ligand by Lewis acid treatment.[130] In contrast, the PLQY of the resulting $[IrAu_{12}(dppe)_5(PA)]^{2+}$ dramatically increased up to 70% by introducing an isocyano-adamantane to the vacant site. These results clearly indicated that dense packing in the ligand layers facilitate the rigidification of the Au_{13} core to improve the PLQY.

3. Doping Effects

This section focuses on the effects of heterometal doping on the PL properties of Au_{13} MPCs. According to the energy gap law,[102,103] broadening of the HOMO-LUMO energy gap is a guiding principle for improving the PLQY. Tuning the electronic structure by heterometal doping is an effective method to change the HOMO/LUMO levels of Au_{13} MPCs.[65–71] So far, group 8 – 12 elements have been successfully doped into the icosahedral Au_{13} core. The formal charge and preferred dopant sites in Au_{13} are listed in Table 1. Doping a heterometal into the Au_{13} core modifies the depth and shape of the jellium potential, leading to an upshift or downshift of the superatomic S, P, and D orbitals, thereby changing the HOMO-LUMO gap of the Au_{13} MPC. Typical examples of the doping effects on the electronic structure and the PL properties are described below. Figures 6 and 7 show the E_{em} and PLQY as a function of E_{HL}, respectively. The data for doped Au_{13} MPCs are shown in lighter tones depending on the ligands while the data for undoped Au_{13} MPCs are shown in brighter tones. As described in the introduction, the total charge z of the doped Au_{13} MPC differs depending on the dopant group to keep the n^* value at 8. Therefore, in the following, the z value is omitted for simplicity.

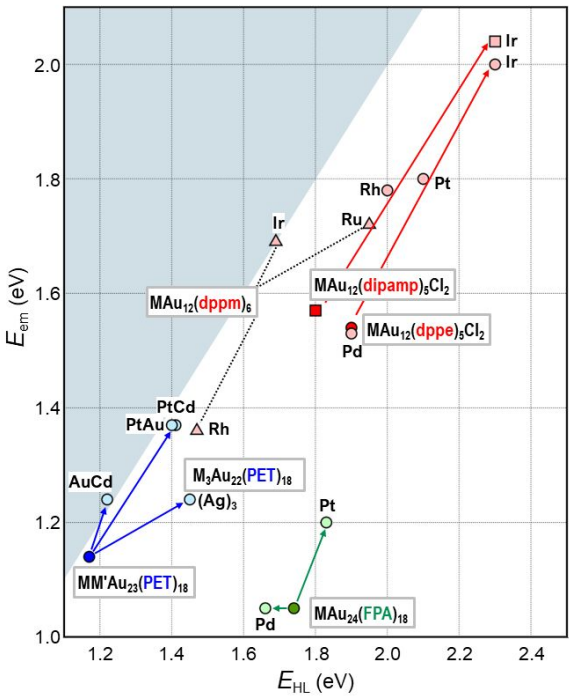

Figure 6. Overview of E_{em} as a function of E_{HL} for doped Au MPCs. Color code for ligands: thiolate (blue), alkynyl (green), phosphine (red). The data for undoped Au_{13} MPCs (M, M' = Au) are shown in brighter tones. The arrows indicate the change in E_{em} and E_{HL} after doping with the respective heterometal.

3.1. X-type Ligands

$MM'Au_{23}(PET)_{18}$ ((M, M') = (Pt, Au), (Au, Cd), (Pt, Cd)): Multi-metal doping can synergistically enhance the PL properties.[89] $PtAu_{24}(PET)_{18}$ had a Pt-centered icosahedral $Pt@Au_{12}$ core.[131] The E_{HL} and E_{em} values of $PtAu_{24}(PET)_{18}$ having a $PtAu_{12}$(8e) core were 1.40 and 1.37 eV, respectively (blue dot in Figure 6), which are significantly larger than those of undoped $Au_{25}(PET)_{18}$ (1.66 and 1.21 eV): the E_{HL} value of 1.17 eV estimated from the optical onset was used for comparison rather than that at 0 K (1.66 eV) estimated from temperature-dependent optical spectra based on the Bose-Einstein model.[108] The PLQY of $PtAu_{24}(PET)_{18}$ was 0.41% (blue dots in Figure 7), ~9 times larger than that of $Au_{25}(PET)_{18}$ (0.048%),[88] due to the increase in E_{HL}. In contrast, the Cd dopant in $CdAu_{24}(PET)_{18}$ was located on the surface of the $Au@Au_{11}Cd$ core and the E_{HL} and E_{em} values were 1.22 and 1.24 eV, respectively (blue dots in Figure 6),[89] comparable to those of undoped $Au_{25}(PET)_{18}$. The PLQY of $CdAu_{24}(PET)_{18}$ (0.27%, blue dot in Figure 7) was ~5 times higher than that of $Au_{25}(PET)_{18}$, due to a larger transition dipole moment from the photoexcited state to the ground state. Interestingly, the Pt- and Cd-codoped cluster $PtCdAu_{23}(PET)_{18}$ had an icosahedral $Pt@Au_{11}Cd$

This journal is © The Royal Society of Chemistry 20xx

Please do not adjust margins

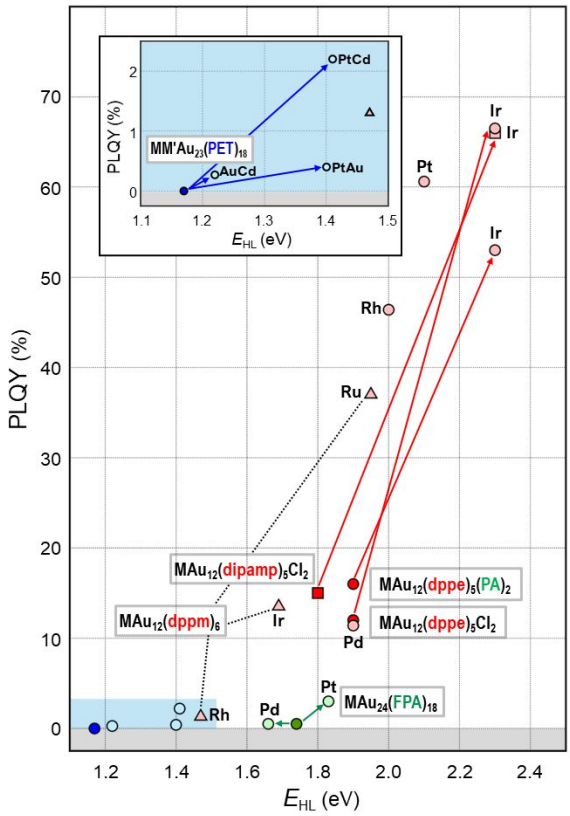

Figure 7. Overview of PLQY as a function of E_{HL} for doped Au MPCs. Color code for ligands: Thiolate (blue), alkynyl (green), phosphine (red). The data points for undoped Au_{13} MPCs (M, M' = Au) are painted in brighter tones. The arrows indicate the change in PLQY and E_{HL} after doping with the respective heterometal.

core and has the E_{HL} and E_{em} values of 1.41 and 1.37 eV, respectively (blue dot in Figure 6). The PLQY of $PtCdAu_{23}(PET)_{18}$ was 2.2%, 46 times higher than that of $Au_{25}(PET)_{18}$. Since the enhancement factor was expressed by the products of those by Pt (×9) and Cd (×5) doping, the PL enhancement was associated with the synergy of two independent mechanisms by Pt and Cd doping.

$Ag_3Au_{22}(PET)_{18}$: In 2013, Kauffman *et al.* reported on $Ag_3Au_{22}(PET)_{18}$, with all 3 Ag atoms occupying positions on the surface to form an $Au@Au_9Ag_3$ icosahedral core.[132] Optical absorption spectroscopy revealed an increase in both E_{HL} (1.45 eV) and E_{em} (1.24 eV) compared to undoped Au_{25} (light blue dot in Figure 6). DFT calculations indicated that the shift was due to an increase in the LUMO energy level, while the HOMO energy level remained unaffected. The PLQYs of $Ag_3Au_{22}(PET)_{18}$ were not reported.

$Ag_xAu_{25-x}(DT)_{18}$ (x ~1, ~4, ~6, ~7, ~9): Negishi succeeded in increasing the number of Ag dopants to $Au_{25}(DT)_{18}$. with an accuracy of ±1 atom.[111] There was an overall trend of increasing E_{HL} and E_{em} with increasing Ag dopant content. In contrast, PLQY varied in the range of 1–4% , with no clear dependence on x observed.

$MAu_{24}(FPA)_{18}$ (M = Au, Pd, Pt): The doping of one Pd atom on $Au_{25}(FPA)_{18}$ decreased the E_{HL} value from 1.74 to 1.66 eV, while Pt doping increased the E_{HL} value from 1.74 to 1.83 eV.[87] The E_{em} value showed little change from 1.05 to 1.06 eV with Pd doping on $Au_{25}(FPA)_{18}$, while it increased to 1.20 eV with Pt doping (light green dots in Figure 6). The Pt-doped cluster has the largest E_{HL} and shows the highest PLQY of 3% in contrast to the undoped or Pd-doped clusters (0.5% each, light green dots in Figure 7), which was due to a large increase in the E_{HL} induced by Pt doping.

3.2. L-type Ligands

$MAu_{12}(dppe)_5Cl_2$ (M = Au, Pt, Pd, Rh, Ir): Doping $Au_{13}(dppe)_5Cl_2$ with a group 9 (Rh, Ir) or group 10 (Pt, Pd) increased the E_{HL} value in the order of 1.9 eV (M = Pd) ≤ 1.9 eV (Au) < 2.0 eV (Rh) < 2.1 eV (Pt) < 2.3 eV (Ir).[91] In accordance with the increase in E_{HL}, the E_{em} was shifted toward higher energies (light red dots in Figure 6): 1.53 eV (M = Pd) < 1.54 eV (Au) < 1.78 eV (Rh) < 1.80 eV (Pt) < 2.00 eV (Ir), and correspondingly, the PLQY increased dramatically (light red dots in Figure 7): 11% (M = Pd) ~12% (Au) < 46% (Rh) < 61% (Pt) < 67% (Ir) under Ar atmosphere. The PL lifetime was also increased in the following order: 2.88 µs (M = Au) < 3.07 µs (Pd) < 5.71 µs (Pt) < 6.03 µs (Ir) < 6.96 µs (Rh), which can be explained by the energy gap law. In the presence of O_2, the PLQYs for M = Rh and Ir were significantly reduced to 0.17 and 0.15% of the initial values, respectively, while that of the undoped clusters remained almost unaffected at 11%. This PL quenching by O_2 indicates that phosphorescence is responsible for the PL of Rh- or Ir-doped clusters.

$MAu_{12}(dppe)_5X_2$ (M = Au, Ir; X = Br, I): The E_{HL} and E_{em} values of $IrAu_{12}(dppe)_5Br_2$ were 2.01 and 1.92 eV, while those of $IrAu_{12}(dppe)_5I_2$ were 2.03 and 1.96 eV, respectively.[100] These values are larger than those for the undoped counterparts (1.85, 1.54 eV) and (1.79, 1.54 eV). Accordingly, the PLQY of $IrAu_{12}(dppe)_5Br_2$ and $IrAu_{12}(dppe)_5I_2$ under Ar atmosphere remarkably increased to 75 and 77%, respectively, from those of the undoped counterparts (10.3 and 6.5%). These QYs of $IrAu_{12}(dppe)_5X_2$ (X = Br, I) are among the highest in MAu_{12} NCs, but are not plotted in Figures 6 and 7 because the doping effects were similar to those of $Au_{13}(dppe)_5Cl_2$. The PL lifetimes of $IrAu_{12}(dppe)_5X_2$ under Ar atmosphere were in the µs order (6.03, 4.90, and 4.15 µs), while they were reduced to 8.04, 7.16, and 6.65 ns for X = Cl, Br, and I, respectively, under air. The PL quenching of $IrAu_{12}(dppe)_5X_2$ by O_2 indicates that a phosphorescence from T_1 state, populated by efficient ISC, is responsible for the radiative decay.

$MAu_{12}(dppe)_5(PA)_2$ (M = Au, Ir): The E_{HL} and E_{em} of $IrAu_{12}(dppe)_5(PA)_2$ were 2.3 eV and 2.02 eV, respectively.[130] The PLQY increased from 16% for $Au_{13}(dppe)_5(PA)_2$ to 53% for $IrAu_{12}(dppe)_5(PA)_2$. Again, the data are not plotted in Figures 6 and 7 for comparison as the doping effect was similar to that in $MAu_{12}(dppe)_5Cl_2$.

$MAu_{12}(R/S\text{-dipamp})_5Cl_2$ (M = Au, Ir): The E_{HL} and E_{em} values of $IrAu_{12}(S\text{-dipamp})_5Cl_2$ were 2.3 and 2.04 eV, respectively (light red square in Figure 6), which are significantly larger than those of undoped $Au_{13}(R/S\text{-dipamp})_5Cl_2$ were 1.9 and 1.57 eV, respectively.[133] As expected from the increased E_{HL}, $IrAu_{12}(S\text{-dipamp})_5Cl_2$ showed a significantly increased PLQY (66%) and PL lifetime (5.87 µs) than those of undoped $Au_{13}(R/S\text{-dipamp})_5Cl_2$ (15%, 3.19 µs) (light red square in Figure 7). $IrAu_{12}(R/S\text{-dipamp})_5Cl_2$ exhibited CPL properties. Although Ir doping did not appreciably enhance the PL anisotropy factors, the brightness of the CPL of $IrAu_{12}(S\text{-dipamp})_5Cl_2$ was five times higher than that of undoped $Au_{13}(S\text{-dipamp})_5Cl_2$. This enhancement in CPL brightness is mainly due to that in the PLQY.

$MAu_{12}(dppm)_6$ (M = Au, Ru, Rh, Ir): Undoped $Au_{13}(dppm)_6$ had a significantly distorted Au_{13} core,[134] whereas $MAu_{12}(dppm)_6$ (M = Ru, Rh, Ir) had an icosahedral M@Au_{12} core.[90] The E_{HL} value increased in the order of 1.47 eV (M = Rh) ≤ 1.69 eV (Ir) < 1.95 eV (Ru). Although $Au_{13}(dppm)_6$ was non-emissive, $MAu_{12}(dppm)_6$ exhibited PL behavior. Consistent with the increase in E_{HL}, the E_{em} was shifted to higher energies (light red triangles in Figure 6): 1.48 eV (M = Rh) < 1.70 eV (Ir) < 1.72 eV (Ru). The PLQY increased dramatically in the order of 1.3% (M = Rh) < 13.5% (Ir) < 37% (Ru) (light red triangles in Figure 7). The PL lifetime of $RuAu_{12}(dppm)_6$ at room temperature decreased from 5.7 μs under Ar to 0.22 μs under ambient conditions, indicating that phosphorescence is responsible for the PL. Interestingly, the PL mechanism of $RuAu_{12}(dppm)_6$ changed to fluorescence at low temperature (<130 K). This temperature dependence was attributed to an energy barrier between the S_1 and T_1 states, which could not be overcome at low temperatures due to the lack of thermal energy.[90]

3.3. Qualitative Explanation of Doping Effects on the PL Properties

Overall, Figure 6 shows that single heterometal atom doping can tune the E_{em} values of the Au_{13} core over the range of 1.1–2.1 eV, a wider range than that achievable by surface modification (Figure 3). In contrast, the Stokes shift is not affected by heterometal doping, as evidenced by an almost equal increase in both E_{em} and E_{HL}. Figure 7 illustrates that the PLQY can be dramatically enhanced to as high as >70% by single heterometal atom doping. We can clearly see in Figure 7 that the correlation between the PLQY and E_{HL} follows the energy gap law:[102,103] the PLQY increases with increase in E_{HL}. Practically, doping of smaller group element (lower valence element) such as Ir is very effective to enhance the PLQY. Previously, we qualitatively explained this trend by a two-step spherical jellium model,[53] which assumes that the host (Au) and dopant atoms provide different background potentials for the confinement of valence electrons. The potential provided by the dopant with lower valency is shallower than that by the Au host element, and vice versa (Table 1, Figure 8). When the smaller group dopant is located at the center of the icosahedral Au_{13} core, the central portion of the jellium potential is upshifted (step ❶ in Figure 8). According to this simple criterion, the 1P orbitals are destabilized by doping a smaller group element in the same period or a smaller period element in the same group with smaller electronegativity. If we assume that the 1D orbitals has larger population near the core center than the 1P orbitals,[135] we can predict that the 1D orbitals are destabilized more than 1P orbitals when upshifting the central portion of the jellium potential by doping a smaller period element (step ❷ in Figure 8). This qualitatively explains why the E_{HL} value of Ir@Au_{12} MPC is obviously larger than that of Au_{13} MPC.

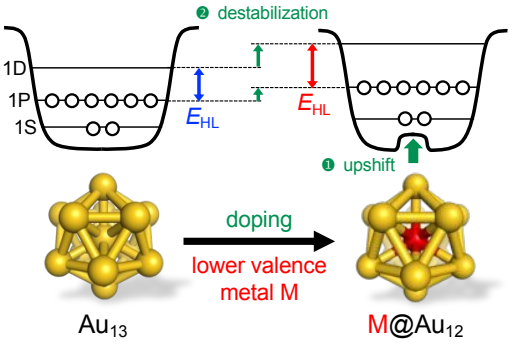

Figure 8. Two-step jellium potential for doping lower valent atoms to Au_{13}.

4. Conclusion and Perspective

In summary, we show that the PL emission energy of Au_{13} MPC can be varied in the range of 1.1–2.1 eV and PL quantum yields (PLQYs) as high as 70% can be realized by proper surface modification and heterometal doping. We can draw the following empirical rules to tune and improve the PL properties of Au_{13} MPC:

(1) The emission wavelength can be blue shifted by using L-type ligands (phosphines, N-heterocyclic carbenes) and/or doping smaller group element such as Ir, Pt, Ru, and Rh.

(2) The PLQY can be enhanced by using L-type ligands (phosphines, N-heterocyclic carbenes) and/or doping smaller group element such as Ir, Pt, Ru, and Rh.

(3) The PLQY can be enhanced by maximizing the interaction between the ligands via π···π or C–H···π interaction, chemical bonding, and steric packing.

(4) Circularly polarized luminescence (CPL) emerged by the structural deformation of the Au_{13} core by chiral ligands.

The first two rules are associated with the expansion of the energy gap between HOMO and LUMO and can be understood qualitatively with a simple scheme based on the jellium model (Figures 5 and 8). However, a more sophisticated theoretical explanation is needed. The third rule is due to the suppression of non-radiative decay by rigidifying the Au core. When the proper interactions between ligands are at work, the independent ligands forming the protective layer act as if they were a single multidentate ligand, thereby limiting the freedom of movement of the Au_{13} core. When the Au_{13} core is in such a protective state, its vibrational frequency increases, reducing the density of vibrational states. As a result, its ability to act as a heat bath for radiation-free relaxation from electronically excited states is reduced. In order to enhance the brightness of CPL, not only PLQY but also dissymmetry factor should be increased by structural deformation by chiral ligands.

Given that the PL quantum yield is governed by the energy gap law,[102,103] the obvious challenge is how to achieve high PL quantum yields in the long wavelength region. In particular, for bioimaging applications, there is a strong need for phosphors that emit efficiently in the NIR-I or NIR-II region, where the penetration into deep tissue is high. So far, Au_{13} clusters emitting in the NIR-II region have been limited to those protected by X-type ligands with very low PLQYs, as illustrated in the upper panel of Figure 9.

This journal is © The Royal Society of Chemistry 20xx

Please do not adjust margins

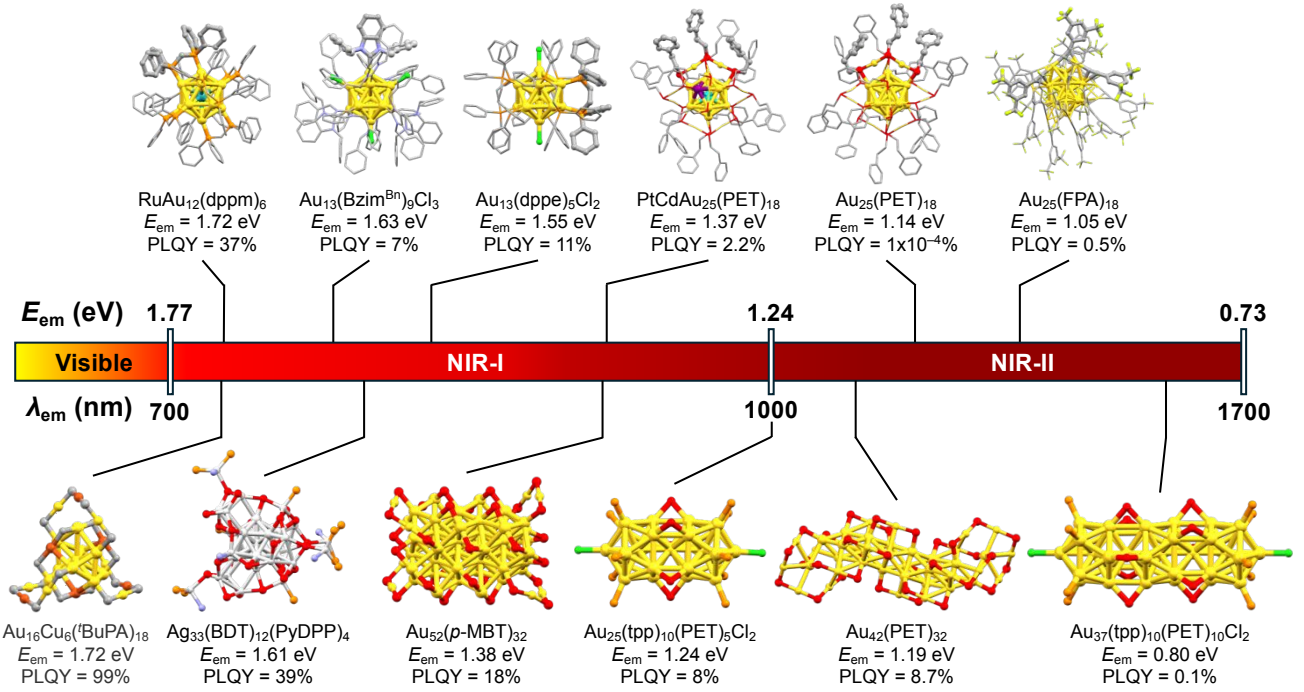

Figure 9. Examples of MPCs showing PL in the NIR I and II region. Color code: Au = yellow, Ag = silver, Ru = turquoise, Pt = light blue, Cd = purple, S = red, Cl = green, P = orange, N = blue, F = light green, C = dark gray. Ligand structures are omitted in the lower panel for simplicity.

However, the PL properties in the NIR-I or NIR-II region can be tuned and improved by controlling other structural parameters such as the nuclearity, morphology, and element of the metal core of MPCs. Actually, there are several examples of non-Au_{13} MPCs with superior PL properties in the NIR-I or NIR-II region, as listed in the lower panel of Figure 9. $[Au_{25}(tpp)_{10}(SC_nH_{2n+1})_5Cl_2]^{2+}$ (n = 2–18) with a bi-icosahedral Au_{25} core[136] had an E_{em} of 1.24 eV and PLQY of 0.1%.[137] The PL of $[Au_{25}(tpp)_{10}(SC_nH_{2n+1})_5Cl_2]^{2+}$ was assigned to phosphorescence.[138] $[Au_{25}(tpp)_{10}(PET)_5Cl_2]^{+}$ had a PLQY of ~8%,[139] while $[Au_{37}(tpp)_{10}(PET)_{10}Cl_2]^{+}$ with a tri-icosahedral Au_{37} core[140] had an E_{em} and PLQY of 0.80 eV and 0.1%, respectively.[139] $Au_{42}(PET)_{32}$ with a rod-like Au_{20} core with an aspect ratio of 6.2 also exhibited dual emission with E_{em} of 1.41 eV and 1.19 eV. These PLs correspond to fluorescence and phosphorescence with PLQYs of 3.2% and 8.7%, respectively.[141] When this Au MPC was embedded in polystyrene films, the PLQY of phosphorescence increased to 20.3%, while the PLQY of fluorescence decreased to 1.1%. The PLQYs of $Au_{52}(SR)_{32}$ ranged from 4 to 18% depending on the steric demand of the ligands:[142] Au_{52}(*p*-MBT)$_{32}$ (*p*-MBT: *p*-methylbenzenethiolate) had an E_{em} of 1.38 eV with a PLQY of 18%. Recently, Wang reported that $Au_{16}Cu_6(^tBuPA)_{18}$ (^{t}BuPA = ^{t}BuPhC≡C) exhibited remarkably bright PL in the NIR-I region.[143] The E_{em} and PLQY were 1.72 eV and 95%, respectively, under ambient conditions. Impressively, the PLQY reached >99% under deaerated conditions. The PLQY of $Au_{16}Cu_6(^tBuPA)_{18}$ was significantly higher than that of undoped $Au_{22}(^tBuPA)_{18}$ (9% under air), while the E_{em} value was comparable to that of undoped $Au_{22}(^tBuPA)_{18}$ (E_{em} = 1.79 eV). The authors concluded that Cu doping slowed down the non-radiative decay by ~60 times and accelerated the ISC process by ~300 times. A NIR-emitting Ag MPC was reported by Nakashima.[144] The modification of $[Ag_{29}(BDT)_{12}(tpp)_4]^{3-}$ (BDT: 1,3-benzenedithiol) with Ag(I)-PyDPP complexes (PyDPP: pyridyl-diphenylphosphine) resulted in the formation of $Ag_{33}(BDT)_{12}(PyDPP)_4$. This modification reduced the E_{em} from 1.82 to 1.61 eV and increased the PLQY from 1.4 to 39%. The authors proposed that the involvement of a triplet state is responsible for the intense PL. These examples suggest that bright PL in the NIR I and II regions can be realized by (1) increasing the Au core size, (2) doping more Ag and Cu into the Au core, and/or (3) making the morphology of Au MPCs anisotropic.

Conflicts of interest

There are no conflicts to declare.

Acknowledgements

This work is affiliated with the Carbon to Metal Coating Institute at Queen's University and was partially funded by the NFRF-T program (#NFRFT-2020-00573). This research was supported financially by JST, CREST (Grant No. JPMJCR20B2).

Notes and references

1. R. L. Whetten, J. T. Khoury, M. M. Alvarez, S. Murthy, I. Vezmar, Z. L. Wang, P. W. Stephens, C. L. Cleveland, W. D. Luedtke and U. Landman, Nanocrystal Gold Molecules, *Adv. Mater.* 1996, **8**, 428–433.
2. A. C. Templeton, W. P. Wuelfing and R. W. Murray, Monolayer-Protected Cluster Molecules, *Acc. Chem. Res.* 2000, **33**, 27–36.

3. H. Qian, M. Zhu, Z. Wu and R. Jin, Quantum Sized Gold Nanoclusters with Atomic Precision, *Acc. Chem. Res.*, 2012, **45**, 1470–1479.
4. P. Maity, S. Xie, M. Yamauchi and T. Tsukuda, Stabilized Gold Clusters: From Isolation Toward Controlled Synthesis, *Nanoscale*, 2012, **4**, 4027–4037.
5. T. Tsukuda, Toward an Atomic-Level Understanding of Size-Specific Properties of Protected and Stabilized Gold Clusters, *Bull. Chem. Soc. Jpn.*, 2012, **85**, 151–168.
6. T. Tsukuda and H. Häkkinen, *Protected Metal Clusters: From Fundamentals to Applications*, 1st ed.; Elsevier: Amsterdam, 2015.
7. R. Jin, C. Zeng, M. Zhou and Y. Chen, Atomically Precise Colloidal Metal Nanoclusters and Nanoparticles: Fundamentals and Opportunities, *Chem. Rev.*, 2016, **116**, 10346–10413.
8. I. Chakraborty and T. Pradeep, Atomically Precise Clusters of Noble Metals: Emerging Link between Atoms and Nanoparticles, *Chem. Rev.*, 2017, **117**, 8208–8271.
9. T. Higaki, Q. Li, M. Zhou, S. Zhao, Y. Li, S. Li and R. Jin, Toward the Tailoring Chemistry of Metal Nanoclusters for Enhancing Functionalities, *Acc. Chem. Res.*, 2018, **51**, 2764–2773.
10. S. Li, N.-N. Li, X.-Y. Dong, S.-Q. Zang and T. C. W. Mak. Chemical Flexibility of Atomically Precise Metal Clusters. *Chem. Rev.,* 2024, **124**, 7262–7378.
11. S. Knoppe and T. Bürgi, Chirality in Thiolate-Protected Gold Clusters, *Acc. Chem. Res.*, 2014, **47**, 1318–1326.
12. N. Goswami, Q. Yao, Z. Luo, J. Li, T. Chen and J. Xie, Luminescent Metal Nanoclusters with Aggregation-Induced Emission, *J. Phys. Chem. Lett.*, 2016, **7**, 962–975.
13. A. Cantelli, G. Guidetti, J. Manzi, V. Caponetti and M. Montalti, Towards Ultra-Bright Gold Nanoclusters, *Eur. J. Inorg. Chem.*, 2017, 5068–5084.
14. C. M. Aikens, Electronic and Geometric Structure, Optical Properties, and Excited State Behavior in Atomically Precise Thiolate-Stabilized Noble Metal Nanoclusters, *Acc. Chem. Res.*, 2018, **51**, 3065–3073.
15. X. Kang and M. Zhu, Tailoring the Photoluminescence of Atomically Precise Nanoclusters, *Chem. Soc. Rev.*, 2019, **48**, 2422–2457.
16. H. Yu, B. Rao, W. Jiang, S. Yang and M. Zhu, The Photoluminescent Metal Nanoclusters with Atomic Precision, *Coord. Chem. Rev.*, 2019, **378**, 595–617.
17. Y. Zhu, J. Guo, X. Qiu, S. Zhao and Z. Tang, Optical Activity of Chiral Metal Nanoclusters, *Acc. Mater. Res.*, 2021, **2**, 21–35.
18. S. Qian, Z. Wang, Z. Zuo, X. Wang, Q. Wang and X. Yuan, Engineering Luminescent Metal Nanoclusters for Sensing Applications, *Coord. Chem. Rev.*, 2022, **451**, 214268.
19. J. Kong, W. Zhang, Y. Wu and M. Zhou, Optical Properties of Gold Nanoclusters Constructed from Au_{13} Units, *Aggregate*, 2022, **3**, e207.
20. D. Cheng, R. Liu and K. Hu, Gold Nanoclusters: Photophysical Properties and Photocatalytic Applications, *Front. Chem.*, 2022, **10**, 958626.
21. K. Bharti, J. K. Sahu and K. K. Sadhu, Origin of Luminescence Properties and Synthetic Methods for Gold- and Bimetallic Gold-Based Nanomaterials, *Mater. Adv.*, 2022, **3**, 5698–5724.
22. Z. Liu, L. Luo and R. Jin, Visible to NIR-II Photoluminescence of Atomically Precise Gold Nanoclusters, *Adv. Mater.*, 2023, 2309073.
23. G. Li and R. Jin, Atomically Precise Gold Nanoclusters as New Model Catalysts, *Acc. Chem. Res.*, 2013, **46**, 1749–1758.
24. Q. Tang, G. Hu, V. Fung and D.-e. Jiang, Insights into Interfaces, Stability, Electronic Properties, and Catalytic Activities of Atomically Precise Metal Nanoclusters from First Principles, *Acc. Chem. Res.*, 2018, **51**, 2793–2802.
25. J. Yan, B. K. Teo and N. Zheng, Surface Chemistry of Atomically Precise Coinage–Metal Nanoclusters: From Structural Control to Surface Reactivity and Catalysis, *Acc. Chem. Res.*, 2018, **51**, 3084–3093.
26. K. Kwak and D. Lee, Electrochemistry of Atomically Precise Metal Nanoclusters, *Acc. Chem. Res.*, 2018, **52**, 12–22.
27. Y. Du, H. Sheng, D. Astruc and M. Zhu, Atomically Precise Noble Metal Nanoclusters as Efficient Catalysts: A Bridge between Structure and Properties, *Chem. Rev.*, 2020, **120**, 526–622.
28. R. Jin, G. Li, S. Sharma, Y. Li and X. Du, Toward Active-Site Tailoring in Heterogeneous Catalysis by Atomically Precise Metal Nanoclusters with Crystallographic Structures, *Chem. Rev.*, 2021, **121**, 567–648.
29. H. Seong and D. Lee, Atomically Precise Metal Nanoclusters for Energy Conversion, *Bull. Korean Chem. Soc.,* 2024, **45**, 435–450.
30. S. Link, A. Beeby, S. FitzGerald, M. A. El-Sayed, T. G. Schaaff and R. L. Whetten, Visible to Infrared Luminescence from a 28-Atom Gold Cluster, *J. Phys. Chem. B*, 2002, **106**, 3410–3415.
31. A. Mooradian, Photoluminescence of Metals, *Phys. Rev. Lett.*, 1969, **22**, 185–187.
32. Y. Tao, M. Li, J. Ren and X. Qu, Metal Nanoclusters: Novel Probes for Diagnostic and Therapeutic Applications, *Chem. Soc. Rev.*, 2015, **44**, 8636–8663.
33. H. Cui, Z.-S. Shao, Z. Song, Y.-B. Wang and H.-S. Wang, Development of Gold Nanoclusters: From Preparation to Applications in the Field of Biomedicine, *J. Mater. Chem. C*, 2020, **8**, 14312–14333.
34. H. Li, H. Li and A. Wan, Luminescent Gold Nanoclusters for *In Vivo* Tumor Imaging, *Analyst*, 2020, **145**, 348–363.
35. J. Tang, H. Shi, G. Ma, L. Luo and Z. Tang, Ultrasmall Au and Ag Nanoclusters for Biomedical Applications: A Review, *Front. Bioeng. Biotechnol.*, 2020, **8**, 1019.
36. S. Zhu, X. Wang, Y. Cong and L. Li, Regulating the Optical Properties of Gold Nanoclusters for Biological Applications, *ACS Omega*, 2020, **5**, 22702–22707.
37. S. M. van de Looij, E. R. Hebels, M. Viola, M. Hembury, S. Oliveira and T. Vermonden, Gold Nanoclusters: Imaging, Therapy, and Theranostic Roles in Biomedical Applications, *Bioconjugate Chem.*, 2022, **33**, 4–23.
38. C. Zhang, X. Gao, W. Chen, M. He, Y. Yu, G. Gao and T. Sun, Advances of Gold Nanoclusters for Bioimaging, *iScience*, 2022, **25**, 105022.
39. X. He, S. Liu, X. Hu, X. Huang, H. Zhang and X. Mao, Precious Metal Clusters as Fundamental Agents in Bioimaging Usability, *Front. Chem.*, 2023, **11**, 1296036.
40. D. Mordini, A. Mavridi-Printezi, A. Menichetti, A. Cantelli, X. Li and M. Montalti, Luminescent Gold Nanoclusters for Bioimaging: Increasing the Ligand Complexity, *Nanomaterials*, 2023, **13**, 648.
41. S. Ni, Y. Liu, S. Tong, S. Li and X. Song, Emerging NIR-II Luminescent Gold Nanoclusters for *in vivo* Bioimaging, *J. Anal. Test.*, 2023, **7**, 260–271.
42. A. Cifuentes-Rius, V. G. Deepagan, J. Xie and N. H. Voelcker, Bright Future of Gold Nanoclusters in Theranostics, *ACS Appl. Mater. Interfaces*, 2021, **13**, 49581-49588.

This journal is © The Royal Society of Chemistry 20xx

Please do not adjust margins

43. K. Sood and A. Shanavas, The Role of Gold Nanoclusters as Emerging Theranostic Agents for Cancer Management, *Curr. Pathobiol. Rep.*, 2021, **9**, 33–42.
44. H. Liu, L. Wang, Z. Xue and X. D. Zhang, Atomic Precise Gold Nanoclusters: Toward the Customize Synthesis, Precision Medicine, *Part. Part. Syst. Char.*, 2023, **40**, 2300084.
45. H. Häkkinen, Atomic and Electronic Structure of Gold Clusters: Understanding Flakes, Cages and Superatoms from Simple Concepts, *Chem. Soc. Rev.*, 2008, **37**, 1847–1859.
46. M. Walter, J. Akola, O. Lopez-Acevedo, P. D. Jadzinsky, G. Calero, C. J. Ackerson, R. L. Whetten, H. Grönbeck and H. Häkkinen, A Unified View of Ligand-Protected Gold Clusters as Superatom Complexes, *Proc. Natl. Acad. Sci. U. S. A.*, 2008, **105**, 9157–9162.
47. Z. Luo and A. W. Castleman, Special and General Superatoms, *Acc. Chem. Res.*, 2014, **47**, 2931–2940.
48. J.-I. Nishigaki, K. Koyasu and T. Tsukuda, Chemically Modified Gold Superatoms and Superatomic Molecules, *Chem. Rec.*, 2014, **14**, 897–909.
49. P. Jena and Q. Sun, Super Atomic Clusters: Design Rules and Potential for Building Blocks of Materials, *Chem. Rev.*, 2018, **118**, 5755–5870.
50. A. Muñoz-Castro, On the Ligand-Core Interaction in Ligand-Protected Gold Superatoms. Insights from $Au_{25}(XR)_{18}$ (X = S, Se, Te) via Relativistic DFT Calculations, *Phys. Chem. Chem. Phys.*, 2019, **21**, 13022–13029.
51. H. Hirai, S. Ito, S. Takano, K. Koyasu and T. Tsukuda, Ligand-Protected Gold/Silver Superatoms: Current Status and Emerging Trends, *Chem. Sci.*, 2020, **11**, 12233–12248.
52. T. Omoda, S. Takano and T. Tsukuda, Toward Controlling the Electronic Structures of Chemically Modified Superatoms of Gold and Silver, *Small*, 2021, **17**, 2001439.
53. S. Takano and T. Tsukuda, Chemically Modified Gold/Silver Superatoms as Artificial Elements at Nanoscale: Design Principles and Synthesis Challenges, *J. Am. Chem. Soc.*, 2021, **143**, 1683–1698.
54. R. Jin, Quantum Sized, Thiolate-Protected Gold Nanoclusters, *Nanoscale*, 2010, **2**, 343–362.
55. W. Kurashige, Y. Niihori, S. Sharma and Y. Negishi, Precise Synthesis, Functionalization and Application of Thiolate-Protected Gold Clusters, *Coord. Chem. Rev.*, 2016, **320–321**, 238–250.
56. X. Kang, H. Chong and M. Zhu, $Au_{25}(SR)_{18}$: The Captain of the Great Nanocluster Ship, *Nanoscale*, 2018, **10**, 10758–10834.
57. Q. Yao, T. Chen, X. Yuan and J. Xie, Toward Total Synthesis of Thiolate-Protected Metal Nanoclusters, *Acc. Chem. Res.*, 2018, **51**, 1338–1348.
58. N. A. Sakthivel and A. Dass, Aromatic Thiolate-Protected Series of Gold Nanomolecules and a Contrary Structural Trend in Size Evolution, *Acc. Chem. Res.*, 2018, **51**, 1774–1783.
59. Z. Lei, X.-K. Wan, S.-F. Yuan, Z.-J. Guan and Q.-M. Wang, Alkynyl Approach toward the Protection of Metal Nanoclusters, *Acc. Chem. Res.*, 2018, **51**, 2465–2474.
60. M.-M. Zhang, X.-Y. Dong, Y.-J. Wang, S.-Q. Zang and T. C. Mak, Recent Progress in Functional Atom-Precise Coinage Metal Clusters Protected by Alkynyl Ligands, *Coord. Chem. Rev.*, 2022, **453**, 214315.
61. K. Konishi, in *Gold Clusters, Colloids and Nanoparticles I*, ed. D. M. P. Mingos, Springer International Publishing, Cham, 2014, pp. 49–86.
62. R. H. Adnan, J. M. L. Madridejos, A. S. Alotabi, G. F. Metha and G. G. Andersson, A Review of State of the Art in Phosphine Ligated Gold Clusters and Application in Catalysis, *Adv. Sci.*, 2022, **9**, 2105692.
63. H. Shen, G. Tian, Z. Xu, L. Wang, Q. Wu, Y. Zhang, B. K. Teo and N. Zheng, N-heterocyclic Carbene Coordinated Metal Nanoparticles and Nanoclusters, *Coord. Chem. Rev.*, 2022, **458**, 214425.
64. E. L. Albright, T. I. Levchenko, V. K. Kulkarni, A. I. Sullivan, J. F. DeJesus, S. Malola, S. Takano, M. Nambo, K. Stamplecoskie, H. Häkkinen, T. Tsukuda and C. M. Crudden, N-Heterocyclic Carbene-Stabilized Atomically Precise Metal Nanoclusters, *J. Am. Chem. Soc.*, 2024, **146**, 5759–5780.
65. R. Jin and K. Nobusada, Doping and Alloying in Atomically Precise Gold Nanoparticles, *Nano Res.*, 2014, **7**, 285–300.
66. Z. Gan, N. Xia and Z. Wu, Discovery, Mechanism, and Application of Antigalvanic Reaction, *Acc. Chem. Res*., 2018, **51**, 2774–2783.
67. S. Wang, Q. Li, X. Kang and M. Zhu, Customizing the Structure, Composition, and Properties of Alloy Nanoclusters by Metal Exchange, *Acc. Chem. Res.*, 2018, **51**, 2784–2792.
68. A. Ghosh, O. F. Mohammed and O. M. Bakr, Atomic-Level Doping of Metal Clusters, *Acc. Chem. Res.*, 2018, **51**, 3094–3103.
69. S. Hossain, Y. Niihori, L. V. Nair, B. Kumar, W. Kurashige and Y. Negishi, Alloy Clusters: Precise Synthesis and Mixing Effects, *Acc. Chem. Res.*, 2018, **51**, 3114–3124.
70. X. Kang, Y. Li, M. Zhu and R. Jin, Atomically Precise Alloy Nanoclusters: Syntheses, Structures, and Properties, *Chem. Soc. Rev.*, 2020, **49**, 6443–6514.
71. T. Kawawaki, Y. Imai, D. Suzuki, S. Kato, I. Kobayashi, T. Suzuki, R. Kaneko, S. Hossain and Y. Negishi, Atomically Precise Alloy Nanoclusters, *Chem. Eur. J.*, 2020, **26**, 16150–16193.
72. M. W. Heaven, A. Dass, P. S. White, K. M. Holt and R. W. Murray, Crystal Structure of the Gold Nanoparticle $[N(C_8H_{17})_4][Au_{25}(SCH_2CH_2Ph)_{18}]$, *J. Am. Chem. Soc.*, 2008, **130**, 3754–3755.
73. M. Zhu, C. M. Aikens, F. J. Hollander, G. C. Schatz and R. Jin, Correlating the Crystal Structure of a Thiol-Protected Au_{25} Cluster and Optical Properties, *J. Am. Chem. Soc.*, 2008, **130**, 5883–5885.
74. J.-J. Li, Z.-J. Guan, Z. Lei, F. Hu and Q.-M. Wang, Same Magic Number but Different Arrangement: Alkynyl-Protected Au_{25} with D_3 Symmetry, *Angew. Chem. Int. Ed.*, 2019, **58**, 1083–1087.
75. Y. Shichibu and K. Konishi, HCl-Induced Nuclearity Convergence in Diphosphine-Protected Ultrasmall Gold Clusters: A Novel Synthetic Route to "Magic-Number" Au_{13} Clusters, *Small*, 2010, **6**, 1216–1220.
76. M. R. Narouz, S. Takano, P. A. Lummis, T. I. Levchenko, A. Nazemi, S. Kaappa, S. Malola, G. Yousefalizadeh, L. A. Calhoun, K. G. Stamplecoskie, H. Häkkinen, T. Tsukuda and C. M. Crudden, Robust, Highly Luminescent Au_{13} Superatoms Protected by N-Heterocyclic Carbenes, *J. Am. Chem. Soc.*, 2019, **141**, 14997–15002.
77. H. Shen, S. Xiang, Z. Xu, C. Liu, X. Li, C. Sun, S. Lin, B. K. Teo and N. Zheng, Superatomic Au_{13} Clusters Ligated by Different N-Heterocyclic Carbenes and their Ligand-Dependent Catalysis, Photoluminescence, and Proton Sensitivity, *Nano Res.*, 2020, **13**, 1908–1911.
78. H. Yi, K. M. Osten, T. I. Levchenko, A. J. Veinot, Y. Aramaki, T. Ooi, M. Nambo and C. M. Crudden, Synthesis and Enantioseparation of Chiral Au_{13} Nanoclusters Protected by

bis-N-Heterocyclic Carbene Ligands, *Chem. Sci.*, 2021, **12**, 10436–10440.

79. M. Laupp and J. Strähle, $[(Ph_3PAu)_6(dppeAu_2)(AuCl)_4Pd]$, an Icosahedral Au_{12} Cluster with a Central Pd Atom, *Angew. Chem. Int. Ed. Engl.*, 1994, **33**, 207–209.
80. S. L. Christensen, M. A. MacDonald, A. Chatt, P. Zhang, H. Qian and R. Jin, Dopant Locaton, Local Structure, and Electronic Properties of $Au_{24}Pt(SR)_{18}$ Nanoclusters, *J. Phys. Chem. C*, 2012, **116**, 26932–26937.
81. C. Kumara, C. M. Aikens and A. Dass X-ray Crystal Structure and Theoretical Analysis of $Au_{25-x}Ag_x(SCH_2CH_2Ph)_{18}^-$ Alloy, *J. Phys. Chem. Lett.*, 2014, **5**, 461–466.
82. S. Yamazoe, W. Kurashige, K. Nobusada, Y. Negishi and T. Tsukuda, Preferential Location of Coinage Metal Dopants (M = Ag or Cu) in $[Au_{25-x}M_x(SC_2H_4Ph)_{18}]^-$ (x~1) as Determined by Extended X-ray Absorption Fine Structure and Density Functional Theory Calculations, *J. Phys. Chem. C*, 2014, **118**, 25284–25290.
83. M. A. Tofanelli, T. W. Ni, B. D. Phillips and C. J. Ackerson, Crystal Structure of the $PdAu_{24}(SR)_{18}^0$ Superatom, *Inorg. Chem.*, 2016, **55**, 999–1001.
84. S. Tian, L. Liao, J. Yuan, C. Yao, J. Chen, J. Yang and Z. Wu, Structures and Magnetism of Mono-Pallidium and Mono-Platinum Doped $Au_{25}(PET)_{18}$ Nanoclusters, *Chem Commun.*, 2016, **52**, 9873–9876.
85. S. Sharma, S. Yamazoe, T. Ono, W. Kurashige, Y. Niihori, K. Nobusada, T. Tsukuda and Y. Negishi, Tuning the Electronic Structure of Thiolate-Protected 25-Atom Clusters by Co-Substitution with Metals Having Different Preferential Site, *Dalton Trans.,* 2016, **45**, 18064–18068.
86. S. Takano, S. Ito and T. Tsukuda, Efficient and Selective Conversion of Phosphine-Protected $(MAu_8)^{2+}$ (M = Pd, Pt) Superatoms to Thiolate-Protected $(MAu_{12})^{6+}$ or Alkynyl-Protected $(MAu_{12})^{4+}$ Superatoms via Hydride Doping, *J. Am. Chem. Soc.*, 2019, **141**, 15994–16002.
87. W. Fei, S. Antonello, T. Dainese, A. Dolmella, M. Lahtinen, K. Rissanen, A. Venzo and F. Maran, Metal Doping of $Au_{25}(SR)_{18}^-$ Clusters: Insights and Hindsights, *J. Am. Chem. Soc.*, 2019, **141**, 16033–16045.
88. M. Suyama, S. Takano and T. Tsukuda, Synergistic Effects of Pt and Cd Codoping to Icosahedral Au_{13} Superatoms, *J. Phys. Chem. C*, 2020, **124**, 23923–23929.
89. H. Hirai, S. Takano, T. Nakamura and T. Tsukuda, Understanding Doping Effects on Electronic Structures of Gold Superatoms: A Case Study of Diphosphine-Protected $M@Au_{12}$ (M = Au, Pt, Ir), *Inorg. Chem.*, 2020, **59**, 17889–17895.
90. S. Takano, H. Hirai, T. Nakashima, T. Iwasa, T. Taketsugu and T. Tsukuda, Photoluminescence of Doped Superatoms $M@Au_{12}$ (M = Ru, Rh, Ir) Homoleptically Capped by $(Ph_2)PCH_2P(Ph_2)$: Efficient Room-Temperature Phosphorescence from $Ru@Au_{12}$, *J. Am. Chem. Soc.*, 2021, **143**, 10560–10564.
91. H. Hirai, S. Takano, T. Nakashima, T. Iwasa, T. Taketsugu and T. Tsukuda, Doping-Mediated Energy-Level Engineering of $M@Au_{12}$ Superatoms (M = Pd, Pt, Rh, Ir) for Efficient Photoluminescence and Photocatalysis, *Angew. Chem. Int. Ed.*, 2022, **61**, e202207290.
92. S. Takano, E. Ito, T. Nakamura and T. Tsukuda, Effect of Group-10 Element M (Ni, Pd, Pt) on Electronic Structure of Icosahedral $M@Au_{12}$ Cores of $MAu_{24}L_{18}$ (L = Alkynyl, Thiolate), *J. Phys. Chem. C*, 2023, **127**, 4360–4366.
93. G. Yousefalizadeh and K. G. Stamplecoskie, A Single Model for the Excited-State Dynamics of $Au_{18}(SR)_{14}$ and $Au_{25}(SR)_{18}$ Clusters, *J. Phys. Chem. A*, 2018, **122**, 7014–7022.
94. M. Zhou and Y. Song, Origins of Visible and Near-Infrared Emissions in $[Au_{25}(SR)_{18}]^-$ Nanoclusters, *J. Phys. Chem. Lett*, 2021, **12**, 1514–1519.
95. K. Yoshida, D. Arima and M. Mitsui, Dissecting the Triplet-State Properties and Intersystem Crossing Mechanism of the Ligand-Protected Au_{13} Superatom, *J. Phys. Chem. Lett.*, 2023, **14**, 10967–10973.
96. H. Kawasaki, S. Kumar, G. Li, C. Zeng, D. R. Kauffman, J. Yoshimoto, Y. Iwasaki and R. Jin, Genration of Singlet Oxygen by Photoexcited $Au_{25}(SR)_{18}$ Clusters, *Chem. Mater.*, 2014, **26**, 2777–2788.
97. S. Wang, L. Tang, B. Cai, Z. Yin, Y. Li, L. Xiong, X. Kang, J. Xuan, Y. Pei and M. Zhu, Ligand Modification of Au_{25} Nanoclusters for Near-Infrared Photocatalytic Oxydative Functionalization, *J. Am. Chem. Soc.*, 2022, **144**, 3787–3792.
98. K. Isozaki, K. Iseri, R. Saito, K. Ueda and M. Nakamura, Dual Catalysis of Gold Nanoclusters: Photocatalytic Cross-Dehydrogenative Coupling by Cooperation of Superatomic Core and Molecularly Modified Staples, *Angew. Chem. Int. Ed.*, 2024, **63**, e202312135.
99. Y. Niihori, T. Kosaka and Y. Negishi, Triplet–Triplet Annihilation-Based Photon Upconversion Using Nanoparticles and Nanoclusters, *Mater. Horiz.*, 2024, **11**, 2304–2322.
100. H. Hirai, S. Takano, S. Masuda and T. Tsukuda, Introducing Iodide Ligands on $IrAu_{12}$ Cluster Enhances Phosphorescence Efficiency and Photoredox Activity, *ChemElectroChem*, 2024, **11**, e202300669.
101. R. Saito, K. Isozaki, Y. Mizuhara and M. Nakamura, Synthesis of N_2-type Superatomic Molecules, *J. Am. Chem. Soc.*, 2024, **146**, 20930–20936.
102. R. Englman and J. Jortner, The Energy Gap Law for Non-Radiative Decay in Large Molecules, *J. Lumin.*, 1970, **1**, 134–142.
103. S. J. Jang, A Simple Generalization of the Energy Gap Law for Nonradiative Processes, *J. Chem. Phys.*, 2021, **155**, 164106.
104. Y. Negishi, K. Nobusada, T. Tsukuda, Glutathione-Protected Gold Clusters Revisited: Bridging the Gap between Gold(I)-Thiolate Complexes and Thiolate-Protected Gold Nanocrystals, *J. Am. Chem. Soc.*, 2005, **127**, 5261–5270.
105. J. F. Parker, C. A. Fields-Zinna and R. W. Murray, The Story of a Monodisperse Gold Nanoparticle: $Au_{25}L_{18}$, *Acc. Chem. Res.*, 2010, **43**, 1289–1296.
106. Z. Wu and R. Jin, On the Ligand's Role in the Fluorescence of Gold Nanoclusters, *Nano Lett.*, 2010, **10**, 2568–2573.
107. J. Akola, M. Walter, R. L. Whetten, H. Häkkinen and H. Grönbeck, On the Structure of Thiolate-Protected Au_{25}, *J. Am. Chem. Soc.*, 2008, **130**, 3756–3757.
108. Z. Liu, Y. Li, E. Kahng, S. Xue, X. Du, S. Li and R. Jin, Tailoring the Electron–Phonon Interaction in $Au_{25}(SR)_{18}$ Nanoclusters via Ligand Engineering and Insight into Luminescence, *ACS Nano*, 2022, **16**, 18448–18458.
109. K. L. D. M. Weerawardene and C. M. Aikens, Theoretical Insights into the Origin of Photoluminescence of $Au_{25}(SR)_{18}^-$ Nanoparticles, *J. Am. Chem. Soc.*, 2016, **138**, 11202–11210.
110. S. Antonello, T. Dainese, M. De Nardi, L. Perotti and F. Maran, Insights into the Interface Between the Electrolytic Solution and The Gold Core in Molecular Au_{25} Clusters, *ChemElectroChem*, 2016, **3**, 1237–1244.

This journal is © The Royal Society of Chemistry 20xx

Please do not adjust margins

111. Y. Negishi, T. Iwai and M. Ide, Continuous Modulation of Electronic Structure of Stable Thiolate-Protected Au_{25} Cluster by Ag doping, *Chem. Commun.*, 2010, **46**, 4713–4715.
112. Y. Song, J. Zhong, S. Yang, S. Wang, T. Cao, J. Zhang, P. Li, D. Hu, Y. Pei and M. Zhu, Crystal Structure of $Au_{25}(SePh)_{18}$ Nanoclusters and Insights into their Electronic, Optical and Catalytic Properties, *Nanoscale*, 2014, **6**, 13977–13985.
113. C. E. Briant, B. R. C. Theobald, J. W. White, L. K. Bell, D. M. P. Mingos and A. J. Welch, Synthesis and X-ray Structural Characterization of the Centred Icosahedral Gold Cluster Compound $[Au_{13}(PMe_2Ph)_{10}Cl_2](PF_6)_3$; the Realization of a Theoretical Prediction, *J. Chem. Soc., Chem. Commun.*, 1981, 201–202.
114. R. C. B. Copley and D. M. P. Mingos, Synthesis and Characterization of the Centred Icosahedral Cluster Series $[Au_9M^{IB}{}_4Cl_4(PMePh_2)_8][C_2B_9H_{12}]$, where M^{IB} = Au, Ag or Cu, *J. Chem. Soc., Dalton Trans.*, 1996, 491–500.
115. Y. Shichibu, K. Suzuki and K. Konishi, Facile Synthesis and Optical Properties of Magic-Number Au_{13} Clusters, *Nanoscale*, 2012, **4**, 4125–4129.
116. M. Sugiuchi, Y. Shichibu, T. Nakanishi, Y. Hasegawa and K. Konishi, Cluster–π Electronic Interaction in a Superatomic Au_{13} Cluster Bearing σ-bonded Acetylide Ligands, *Chem. Commun.*, 2015, **51**, 13519–13522.
117. Z.-H. Gao, J. Dong, Q.-F. Zhang and L.-S. Wang, Halogen Effects on the Electronic and Optical Properties of Au_{13} Nanoclusters, *Nanoscale Adv.*, 2020, **2**, 4902–4907.
118. N. Kito, S. Takano, S. Masuda, K. Harano and T. Tsukuda, Au_{13} Superatom Bearing Two Terpyridines at Coaxial Positions: Photoluminescence Quenching via Complexation with 3d Metal Ions, *Bull. Chem. Soc. Jpn.*, 2023, **96**, 1045–1051.
119. Y. Yang, Q. Zhang, Z.-J. Guan, Z.-A. Nan, J.-Q. Wang, T. Jia and W.-W. Zhan, Enantioselective Synthesis of Homochiral Au_{13} Nanoclusters and Their Chiroptical Activities, *Inorg. Chem.*, 2019, **58**, 3670–3675.
120. Y. Shichibu, Y. Ogawa, M. Sugiuchi and K. Konishi, Chiroptical Activity of Au_{13} Clusters: Experimental and Theoretical Understanding of the Origin of Helical Charge Movements, *Nanoscale Adv.*, 2021, **3**, 1005–1011.
121. J.-H. Yu, Z.-R. Yuan, J. Xu, J.-G. Wang, M. Azam, T.-D. Li, Y.-Z. Li and D. Sun, Monoarsine-protected Icosahedral Cluster $[Au_{13}(AsPh_3)_8Cl_4]^+$: Comparative Studies on Ligand Effect and Surface Reactivity with its Stibine Analogue, *Chem. Sci.*, 2023, **14**, 6564–6571.
122. Y. Shichibu, F. Zhang, Y. Chen, M. Konishi, S. Tanaka, H. Imoto, K. Naka and K. Konishi, Diarsine- vs Diphosphine-protected Au_{13} clusters: Effect of Subtle Geometric Differences on Optical Property and Electronic Structure, *J. Chem. Phys.*, 2021, **155**, 054301.
123. Y.-Z. Li, R. Ganguly, K. Y. Hong, Y. Li, M. E. Tessensohn, R. Webster and W. K. Leong, Stibine-Protected Au_{13} Nanoclusters: Syntheses, Properties and Facile Conversion to GSH-protected Au_{25} Nanocluster, *Chem. Sci.*, 2018, **9**, 8723–8730.
124. M. R. Narouz, K. M. Osten, P. J. Unsworth, R. W. Y. Man, K. Salorinne, S. Takano, R. Tomihara, S. Kaappa, S. Malola, C.-T. Dinh, J. D. Padmos, K. Ayoo, P. J. Garrett, M. Nambo, J. H. Horton, E. H. Sargent, H. Häkkinen, T. Tsukuda, C. M. Crudden, *N*-Heterocyclic Carbene-Functionalized Magic Number Gold Nanoclusters. *Nature Chem.* **2019**, *11*, 419-425.
125. P. Luo, X.-J. Zhai, S. Bai, Y.-B. Si, X.-Y. Dong, Y.-F. Han and S.-Q. Zang, Highly Efficient Circularly Polarized Luminescence from Chiral Au_{13} Clusters Stabilized by Enantiopure Monodentate NHC Ligands, *Angew. Chem. Int. Ed.*, 2023, **62**, e202219017.
126. X. Wang, R. Liu, L. Tian, J. Bao, C. Zhao, F. Niu, D. Cheng, Z. Lu and K. Hu, Highly Luminescent NHC-Stabilized Au_{13} Clusters as Efficient Excited-State Electron Donors, *J. Phys. Chem. C*, 2022, **126**, 18374–18382.
127. M. Bevilacqua, M. Roverso, S. Bogialli, C. Graiff and A. Biffis, From Au_{11} to Au_{13}: Tailored Synthesis of Superatomic Di-NHC/PPh_3-Stabilized Molecular Gold Nanoclusters, *Inorg. Chem.*, 2023, **62**, 1383–1393.
128. P. Luo, S. Bai, X. Wang, J. Zhao, Z. N. Yan, Y. F. Han, S. Q. Zang and T. C. Mak, Tuning the Magic Sizes and Optical Properties of Atomically Precise Bidentate N-Heterocyclic Carbene-Protected Gold Nanoclusters via Subtle Change of N-Substituents, *Adv. Opt. Mater.*, 2021, **9**, 2001936.
129. E. L. Albright, S. Malola, S. I. Jacob, H. Yi, S. Takano, K. Mimura, T. Tsukuda, H. Häkkinen, M. Nambo and C. M. Crudden, Enantiopure Chiral Au_{13} Nanoclusters Stabilized by Ditopic N-Heterocyclic Carbenes: Synthesis, Characterization, and Electrocatalytic Reduction of CO_2, *Chem. Mater.*, 2024, **36**, 1279–1289.
130. Y. Fukumoto, T. Omoda, H. Hirai, S. Takano, K. Harano and T. Tsukuda, Diphosphine-Protected $IrAu_{12}$ Superatom with Open Site(s): Synthesis and Programmed Stepwise Assembly, *Angew. Chem. Int. Ed.*, 2024, **63**, e202402025.
131. M. Suyama, S. Takano, T. Nakamura and T. Tsukuda, Stoichiometric Formation of Open-Shell $[PtAu_{24}(SC_2H_4Ph)_{18}]^-$ via Spontaneous Electron Proportionation between $[PtAu_{24}(SC_2H_4Ph)_{18}]^{2-}$ and $[PtAu_{24}(SC_2H_4Ph)_{18}]^0$, *J. Am. Chem. Soc.*, 2019, **141**, 14048–14051.
132. D. R. Kauffman, D. Alfonso, C. Matranga, H. Qian and R. Jin, A Quantum Alloy: The Ligand-Protected $Au_{25-x}Ag_x(SR)_{18}$ Cluster, *J. Phys. Chem. C*, 2013, **117**, 7914–7923.
133. H. Hirai, T. Nakashima, S. Takano, Y. Shichibu, K. Konishi, T. Kawai and T. Tsukuda, $IrAu_{12}$ Superatom Modified by Chiral Diphosphines: Doping-induced Enhancement of Chiroptical Activity, *J. Mater. Chem. C*, 2023, **11**, 3095–3100.
134. S.-S. Zhang, L. Feng, R. D. Senanayake, C. M. Aikens, X.-P. Wang, Q.-Q. Zhao, C.-H. Tung and D. Sun, Diphosphine-protected Ultrasmall Gold Nanoclusters: Opened Icosahedral Au_{13} and Heart-shaped Au_8 clusters, *Chem. Sci.*, 2018, **9**, 1251–1258.
135. J. T. A. Gilmour and N. Gaston, 5-Fold Symmetry in Superatomic Scandium Clusters: Exploiting Favourable Orbital Overlap to Sequester Spin, *Phys. Chem. Chem. Phys*., 2020, **22**, 4051–4058.
136. Y. Shichibu, Y. Negishi, T. Watanabe, N. K. Chaki, H. Kawaguchi and T. Tsukuda, Biicosahedral Gold Clusters $[Au_{25}(PPh_3)_{10}(SC_nH_{2n+1})_5Cl_2]^{2+}$ (n = 2−18): A Stepping Stone to Cluster-Assembled Materials, *J. Phys. Chem. C*, 2007, **111**, 7845–7847.
137. S. Park and D. Lee, Synthesis and Electrochemical and Spectroscopic Characterization of Biicosahedral Au25 Clusters, *Langmuir*, 2012, **28**, 7049–7054.
138. M. Mitsui, Y. Wada, R. Kishii, D. Arima and Y. Niihori, Evidence for Triplet-State-Dominated Luminescence in Biicosahedral Superatomic Molecular Au_{25} Clusters, *Nanoscale*, 2022, **14**, 7974–7979.
139. Q. Li, C. J. Zeman IV, Z. Ma, G. C. Schatz and X. W. Gu, Bright NIR-II Photoluminescence in Rod-Shaped Icosahedral Gold Nanoclusters, *Small*, 2021, **17**, 2007992.
140. R. Jin, C. Liu, S. Zhao, A. Das, H. Xing, C. Gayathri, Y. Xing, N. L. Rosi, R. R. Gil and R. Jin, Tri-icosahedral Gold Nanocluster

$[Au_{37}(PPh_3)_{10}(SC_2H_4Ph)_{10}X_2]^+$: Linear Assembly of Icosahedral Building Blocks, *ACS Nano*, 2015, **9**, 8530–8536.

141. L. Luo, Z. Liu, X. Du and R. Jin, Near-Infrared Dual Emission from the $Au_{42}(SR)_{32}$ Nanocluster and Tailoring of Intersystem Crossing, *J. Am. Chem. Soc.*, 2022, **144**, 19243–19247.
142. Y. Wang, Z. Liu, A. Mazumder, C. G. Gianopoulos, K. Kirschbaum, L. A. Peteanu and R. Jin, Tailoring Carbon Tails of Ligands on $Au_{52}(SR)_{32}$ Nanoclusters Enhances the Near-Infrared Photoluminescence Quantum Yield from 3.8 to 18.3%, *J. Am. Chem. Soc.*, 2023, **145**, 26328–26338.
143. W.-Q. Shi, L. Zeng, R.-L. He, X.-S. Han, Z.-J. Guan, M. Zhou and Q.-M. Wang, Near-unity NIR Phosphorescent Quantum Yield from a Room-Temperature Solvated Metal Nanocluster, *Science*, 2024, **383**, 326–330.
144. W. Ishiii, Y. Okayasu, Y. Kobayashi, R. Tanaka, S. Kato, Y. Nishikawa, T. Kawai and T. Nakashima, Excited State Engineering in Ag_{29} Nanocluster through Peripheral Modification with Silver(I) Complexes for Bright Near-Infrared Photoluminescence, *J. Am. Chem. Soc.*, 2023, **145**, 11236–11244.

This journal is © The Royal Society of Chemistry 20xx

Please do not adjust margins

Dear Prof. Song Gao,

Data availability statement

No primary research results, software or code have been included and no new data were generated or analysed as part of this review.

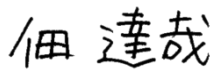

Prof. Tatsuya Tsukuda

Department of Chemistry, Graduate School of Science,
The University of Tokyo
7-3-1 Hongo, Bunkyo-ku, Tokyo 113-0033, Japan
Tel: +81-3-5841-4363
E-mail: tsukuda@chem.s.u-tokyo.ac.jp